Ciemat

Designing a compensating quartz fiber calorimeter for low angle calorimetry at LHC

A. Ferrando
M.C. Fouz
M.I. Josa
A. Khan
A. Rosowsky
J.M. Salicio

Designing a compensating quartz fiber calorimeter for low angle calorimetry at LHC

A. Ferrando
M.C. Fouz
M.I. Josa
A. Khan
A. Rosowsky
J.M. Salicio

Toda correspondencia en relación con este trabajo debe dirigirse al Servicio de Información y Documentación, Centro de Investigaciones Energéticas, Medioambientales y Tecnológicas, Ciudad Universitaria, 28040-MADRID, ESPAÑA.

Las solicitudes de ejemplares deben dirigirse a este mismo Servicio.

Los descriptores se han seleccionado del Thesauro del DOE para describir las materias que contiene este informe con vistas a su recuperación. La catalogación se ha hecho utilizando el documento DOE/TIC-4602 (Rev. 1) Descriptive Cataloguing On-Line, y la clasificación de acuerdo con el documento DOE/TIC.4584-R7 Subject Categories and Scope publicados por el Office of Scientific and Technical Information del Departamento de Energía de los Estados Unidos.

Se autoriza la reproducción de los resúmenes analíticos que aparecen en esta publicación.

CLASIFICACIÓN DOE Y DESCRIPTORES

440500, 430303
CALORIMETERS, CHERENKOV COUNTERS, ACCELERATORS, QUARTZ, DESIGN

"Designing a compensating quartz fiber calorimeter for low angle calorimetry at LHC"

Ferrando, A.; Fouz, M.C.; Josa, M.I.; Khan, A.; Rosowsky, A.; Salicio, J.M.
54 pp. 27 figs. 15 refs.

Abstract

We present a design of a compensating quartz fiber clorimeter, made of a unique active section, and ment for the specific physics requirements of the low angle calorimetry in LHC experiments.

The proposed calorimeter is exemplified for the case of the CMS experiment.

"Diseñando un calorímetro compensante de fibras de cuarzo para" calorimetría a pequeño ángulo en LHC"

Ferrando, A.; Fouz, M.C.; Josa, M.I.; Khan, A.; Rosowsky, A.; Salicio, J.M.
54 pp. 27 figs. 15 refs.

Resumen

Presentamos un diseño de calorímetro compensante basado en fibras de cuarzo, confeccionado con una única sección activa, y expresamente pensado para dar satisfacción a los requisitos específicos de los calorímetros a pequeño ángulo en experimentos LHC.

El calorímetro que se propone se ejemplariza para el caso del experimento CMS.

DESIGNING A COMPENSATING QUARTZ FIBER CALORIMETER FOR LOW ANGLE CALORIMETRY AT LHC

A. Ferrando[1], M.C. Fouz[1,2], M.I. Josa[1], A. Khan[1,#],
A.Rosowsky[3] and J.M. Salicio[1]

CIEMAT[1,*] (Madrid), CERN[2] (Geneva) and SACLAY[3] (Paris)

Abstract

We present a design of a compensating quartz fiber calorimeter, made of a unique active section, and ment for the specific physics requirements of the low angle calorimetry in LHC experiments.

The proposed calorimeter is exemplified for the case of the CMS experiment.

(To be submitted to Nucl. Instr. and Methods A)

1. Introduction

The Very Forward Calorimeters (VFCAL) in CMS [1] cover the pseudorapidity range $3.0 \leq |\eta| \leq 5.0$. The VFCAL is ment to improve the measurement of the missing transverse energy (E_t^{miss}) and also to enable very forward jets identification with good energy reconstruction. These jets are a distinguishing characteristic of several important physics processes.

The measurement of E_t^{miss} is important in the study of top quark production and for Standard Model (SM) Higgs searches with $m_H \geq 500$ GeV in the H -> ZZ -> llvv and H -> WW -> lvjj channels. It is also important in SUSY searches as A -> $\tau\tau$ -> eμ + E_t^{miss} and A -> $\tau\tau$ -> l$^{\pm}$h$^{\pm}$ + E_t^{miss}, allowing the reconstruction of the A mass. Studies of WWγ and WWZ gauge boson couplings and searches for supersymmetric particles are also improved by the presence of the VFCAL.

The production of heavy Higgs boson ($m_H \approx 1$ TeV), through the WW or ZZ fusion mechanism (and subsequent decay H-> WW -> lvjj, H -> ZZ -> lljj), is characterised by the appearance of two forward tagging jets. These jets are energetic ($<p_L> \approx 1$ TeV) and have a transverse momentum of the order of m_W. They are emitted in the pseudorapidity range $2.0 \leq |\eta| \leq 5.0$. The detection of these tagging jets is mandatory in order to suppress the large QCD W, Z + jets background. The detection of forward tagging jets is also useful for the 80 to 140 GeV mass range of the Higgs.

In all the above cases, the performance asked to the VFCAL is not very stringent. The VFCAL is required to have a moderate energy resolution, a sufficiently fine granularity for tagging and angular reconstruction of the forward jets and an acceptable degree of compensation allowing their energy reconstruction.

In addition, the VFCAL is required to have a very fast response time, to be radiation resistant and costless.

A VFCAL, based on quartz fibres technology [2-4], is proposed for covering the low angle regions of CMS [1]. The time response and radiation resistance requirements are fulfilled: collection of light by Cerenkov effect and use of radiation hard materials in its construction.

We present in this document some ideas for the design of a non-segmented, compensating, quartz fiber calorimeter, ment for the specific physics requirements of the low angle calorimetry in the CMS experiment.

Our goal is to design a calorimeter able to provide a response for tagging jets that stays proportional to the jet energy, being at the same time, independent of the electromagnetic composition of the jets.

Such a design, however, must not compromise the jet finding capabilities, the jet energy and angular resolutions.

A *one segment* design would minimize the amount of quartz fibers and the associated electronics, lowering the cost by a significant factor. The mechanical construction and installation get also simplified.

Our study is based on Monte-Carlo calculations. The document is organized as follows: some needed definitions and the bases of the work are given in section 2. The Cerenkov effect in fibers and the simulation used in this study are explained in section 3, while results from the simulation are given in section 4. Finally, we summarize our results and draw some conclusions in section 5.

2. Definitions and the working rules

2.1 Single particles

We shall define compensation for single particles, as the capability of a calorimeter to obtain the same response for electromagnetic (e.m.) and hadronic (had.) showers with the same initial energy. In what follows, we are going to define *degree* or *level of compensation* as

$$C_p = S_e/S_\pi \qquad (1)$$

where S_e (S_π) represents the mean signal collection (charge, light, etc.) obtained with electron (pion) beams of a given energy. A compensating calorimeter will have C_p equal or close to one.

Detailed references to compensation in calorimetry can be found in the literature (see [5-7] as classic examples). We shall follow the definition in eq. (1) for the quantification of the level of compensation for single particles.

In general, since the pion (or, generally, hadron) showers contain a good fraction of undetectable energy, it is normal (but not a rule) that $S_e > S_\pi$ and so, $C_p > 1$. The higher is the deviation from 1, the lower will be the capability of compensation of the device.

For making $C_p \rightarrow 1$, one has two solutions: either S_π is enhanced, or S_e is suppressed.

An example of S_π enhancement can be found in [8]. This reference reports on test beam studies with an uranium/tetrametilpentane (U/TMP) sampling calorimeter. TMP contains plenty of hydrogen molecules. Protons in the warm liquid are recoiled by low energy neutrons in the hadron shower. By

operating the module at a certain voltage, electrons from proton ionization of the liquid can escape from recombination and then enhance the collected signal at the anode. In other words, C_p is *tuned* by the applied high voltage. In the case of the U/TMP calorimeter, it also happens that the energy resolution gets better when increasing the voltage applied, due to the higher number of collected electrons at the anode.

An example of S_e suppression can be found in [9,10]. In this case, the device is an iron/gas sampling calorimeter constructed by the interleave of planes of parallel plate chambers and iron absorber. The gas used in this example does not contain any hydrogen molecules, to avoid any recoiling proton effects, and Cp -> 1 is obtained by using a given sampling fraction (gas gap/iron plate thickness), the same in both e.m. and had. sections. Here, and for a given gap of gas, it is the thickness of the iron plates that is tuning the compensation. The stochastic term in the single particle energy resolution gets degraded as $1/\sqrt{L}$, where L is the iron thickness.

One *software* or *offline* way of obtaining compensation is in the use of *segmented* sampling calorimeters (made of two or more segments). Let us consider two segments such that the first one fully contains the e.m. showers in depth and that the total length of the calorimeter (e.m. plus had. sections) is enough to fully contain the hadronic cascades. In that case (assuming the device has a linear response) we can make C_p -> 1 if one is able to compute two different calibration constants, α and β, for the two different segments in such a way that the reconstructed energy can be written as

$$E_e^r = \alpha \times S_{em} \tag{2}$$

$$E_\pi^r = \alpha \times S_{em} + \beta \times S_{had} \tag{3}$$

and, satisfying

$$E_e^r = E_e^{beam} \tag{4}$$

$$E_\pi^r = E_\pi^{beam} \tag{5}$$

where S_{em} is the signal collected from the e.m. section, E_e^r is the reconstructed energy for electrons, S_{had} is the signal collected in the had. section, E_π^r is the reconstructed energy for pions, E_e^{beam} is the energy of the electron beam and E_π^{beam} is that for pion beam. The calibration constants α and β are obtained by fitting the data measurements to eqs. (2) to (5). This way of doing may (or

may not) degrade the intrinsic pion energy resolution of the calorimeter.

2.2 jets

The specific aims of the low angle calorimetry in LHC experiments, as given in section 1, need the introduction of the concept of compensation when dealing with jets.

In a calorimeter based on the Cerenkov effect in fibers, the signal is essentially provided by the e.m. component of the showers. Hence, in a jet, the content in photons (γ) is a critical issue. Therefore, we define that a quartz fiber sampling calorimeter is compensating for jets, when the response is independent of its electromagnetic composition (the fraction of gammas, whatever is their origin), while keeping the linearity of the response with respect to the the jet energy (*sine qua non* condition for a good energy reconstruction).

2.3 Working rule for the design of a quartz fiber calorimeter giving compensation for both, single particles and jets, and having a unique active section

To get Cp -> 1 and, at the same time, compensation for jets, in a non-segmented quartz fiber calorimeter, we propose a partial suppression of the electromagnetic signal by the use of a given depth of dummy absorber in the front part of the device.

3. The Monte-Carlo simulation of the Cerenkov effect in fibres

3.1 Quartz fiber calorimetry

A charged particle traversing a quartz fiber with a velocity greater than the speed of light in the quartz, emit photons through the Cerenkov effect.

The opening angle of the Cerenkov cone, Θ_c is related with the speed of the particle, β, by the relation:

$$\cos \Theta_c = 1/n\beta \tag{1}$$

where n is the index of refraction of the fiber. There is a β threshold value ($\beta_{min} = 1/n$), below which there is no Cerenkov radiation.

The light yield in photoelectrons (p.e.), due to the Cerenkov effect [11] is given by:

$$d^2N(p.e.)/dxd\lambda = 2\pi\alpha z^2(\sin^2 \Theta_c /\lambda^2) = 2\pi\alpha z^2/\lambda^2 [1-1/\beta^2 n(\lambda)^2] \quad (2)$$

where α is the fine structure constant, Θ_c is the Cerenkov angle, λ is the wavelength of the emitted light, x the path of the particle through the medium and z the charge of the incident particle.

The amount of light *seen* by a detector placed at one end of the fiber will depend on the velocity of the particle (eq. (2)), on the incident angle and on the distance between the particle trajectory and the center of the fiber. It also depends on the fiber core and cladding indices of refraction, on the spectral transmission range of the fiber and on the spectral quantum efficiency of the light detector [4].

The particles entering the absorber of a calorimeter make showers of lower momentum particles. Amongst them, the ones entering in a quartz fiber with β close to 1 are essentially electrons. From the electrons in a shower, the ones producing light in a quartz fiber are roughly those entering in the fiber with an angle of $\approx 45^o \pm 10^o$ [4].

The above consequence is that the *apparent shower development* in fiber calorimeters is dramatically different from the one observed in dE/dx calorimeters: the showers appear to be very narrow. For electron showers, the transverse development is narrower than the Moliere radius of the absorber! Concerning pions, the apparent radial development is roughly in the order of 1/10 of the interaction length of the absorber. In both cases we are referring to a containment of $\approx 90\%$.

Since in a pion (i.e. hadron) shower, secondary electron production is directly related with the π^o and η^o production in the absorber, the light collection in single hadrons showers is dominated by the statistical fluctuations in the production of these particles. The level of compensation, both in single particles and jets, are a priori conditioned by the fact that it is only a part of the e.m. component of the hadron cascade (i.e. jet cascade) that is trapped by the active element (the fibers). The working rule in paragraph 2.3 trys to lessen this effect.

Note that the narrow appearence of the showers may be an advantage for cluster finding of interesting objects, as forward jets, provided that the arrangement of fibers is done as to obtain a fine granularity in the transverse dimensions and that the packing fraction is sufficiently large as to get enough signal at the light detectors. As an example: inserting a quartz fiber short section module ($\approx$ 1 cm in depth) placed between ECAL and HCAL will

complement the inner CMS calorimetry system with a high resolution position detector for jets.

3.2 Simulation of a quartz fiber calorimeter module

For simulation, we have used a simple geometry (see fig. 2): a block of copper as absorber with quartz fibers, running parallel to the beam direction, embedded in it.

We also assume that the fibers have a core made of quartz and a cladding made of a quartz composite. The fibers are disposed such that, in the transverse plane, any three neighbouring fibers are sitting on the vertices of an equal side triangle. This gives the most uniform disposition of fibers inside the absorber.

In the test beam, the section of the fiber core is 0.3 mm of quartz, surrounded by 0.02 mm thick fluoring doped quartz cladding. The numerical aperture of the fibers ($NA = \sqrt{(n_{co}^2 - n_{cl}^2)}$, n_{co} and n_{cl} being the refraction index for core and cladding, respectively)) is then ≈ 0.22.

For shower simulation we have used GEANT 3.21 [12], modified so as to simulate the light production and propagation due to the Cerenkov effect in fibers.

To compute the number of p.e., we integrate eq. (2) in the interval 300 nm $< \lambda <$ 600 nm (corresponding to the quartz transparency and the working range of the PMs currently in use in the test beam). Once integrated, for every GEANT step eq. (2) takes the form:

$$N = C\,L \qquad\qquad\qquad (3)$$

where L represents the GEANT path segment travelled in the fibers quartz core and C is the product of the remaining terms in eq. (2). C is computed for each GEANT segment. Its value is very small, typically in the 10^{-4} and eq. (3), is dominated by statistical fluctuations Poisson-like. This is why, in our simulation, we aproximate N, in eq. (3) by randomly generating a number from a Poisson distribution having CL as mean value.

Convenient reduction factors take into account the absorbed light due to the NA, the quartz transparency and the quantum efficiency of the PMs.

4. Results from simulation

4.1 Single particles

For single particles we have used a geometry as in fig. 2, with 15 x 15 cm^2 transverse dimensions and a total depth, including the dummy absorber, of 1350 mm ($\approx$ 9 λ_I). These dimensions are enough to fully contain electrons and pions. The transverse distance between neighbouring fibers is 2.3 mm and the fibers section is 0.3 mm. For this study, the thickness of the dummy part is expressed in terms of number of radiation lengths, from 0 Xo (full module active) to 10 Xo. In what follows we will refer to this thickness as, n Xo cut (n = 0, ..., 10). We generated 1000 showers of electrons and pions for a number of energy points with the 11 geometrical scenarios.

The longitudinal shower profiles, in copper, are presented for electrons (continuous line) and pions (dashed line) in figs. 3 a) and b) for energies of 100 GeV and 500 GeV, respectively. The maximum of the electron showers is found around 8 - 9 Xo in depth.

The distribution of the collected light, expressed in number of photo-electrons (p.e.), for 100 GeV and 350 GeV electrons are shown, as an example, in fig. 4 a) and b), respectively, for various cut values. A Gaussian fit is superimposed to the simulated data. It can be seen that the signal diminishes with cuts while the Gaussian shapes are conserved. The same distributions for pions are shown in figs. 5 a) and b). We observe that the pion signal diminishes slower than for electron while maintaining the Gaussian shape.

The level of compensation, C_p, as a function of the particle energy is presented in fig. 6 for the various cuts. The average value of C_p, for particles in the range 200 GeV - 500 GeV is shown in fig. 7 as a function of the cut. Reasonable values for Cp are observed in the region 7 to 9 Xo cut.

Linearity plots are shown in figs. 8 and 9 for electrons and pions respectively. In these figures, the fitted mean value for the collected signal is plotted as a function of the energy of the incoming particle, for the various cuts considered (from none to 10 Xo). Data points are fitted to the form

$$S \text{ (p.e.)} = \alpha \times E \text{ (GeV)} + \beta \tag{6}$$

The slopes vary from 0.71 p.e./GeV (0 Xo cut) to 0.40 p.e./GeV (10 Xo) for electrons while for pions they are in the interval 0.45 to 0.42 p.e/GeV. The complete sets of the fitted α

and β values are shown in figs. 10 and 11 for electrons and pions, respectively. As expected, the slope decrease dramatically with the Xo cut in the case of electron showers, while stays roughly constant for pion cascades.

The energy resolutions as a function of the particle energy, are shown in figs. 12 and 13 for electrons and pions, respectively. Each plot in these figures corresponds to a given Xo cut. Simulated data points are fitted to

$$\sigma(E)/E = a/\sqrt{E} + b \qquad (7)$$

The fitted values for stochastic (full circles) and constant (open circles) terms, for the various cuts, are compared in figs. 14 a) and b), for electrons and pions respectively. No dramatic deterioration of the energy resolution is observed. To quantify the effect, we give in figs. 15 a) and b) the energy resolution for 100 GeV (full circles) and 500 GeV (open circles) electrons and pions, respectively, as a function of the Xo cut. As observed in fig. 15 a), and comparing the points at 0 Xo and 8 Xo, the electron energy resolution degrades from 12% to 18% for 100 GeV and from 5% to 9% for 500 GeV. No significant degradation of the pion energy resolution is seen (fig. 15 b)).

4.2 Jets

We have used a sample of 1260 tagging jets from the reaction qq' -> (WW, ZZ ->H) jj' (see section 1). Particles from jets were swimmed from the interaction point to the assumed position of the VFCAL front face ($\approx$ 11 m), in the CMS scenario. Details about event generation and tracking of particles in a jet, through the 4 T magnetic field, to the very forward region can be found in ref. [13]. For VFCAL we have used the same geometry as in section 4.1. Now, the simulated module has 3 x 3 m^2 transverse dimensions and the same 9 λ_I depth.

The energy distribution of the jets in the sample is shown in fig. 16 a). They cover the region from 500 GeV to 3 TeV. Their electromagnetic composition (γ fraction = #gammas/total multiplicity in the jet) is shown in fig. 16 b).

We have checked that there is no correlation between the γ fraction in a jet and the jet energy (fig. 17).

Particles in the jets are fully simulated in the calorimeter. The linearity of the response, in terms of collected signal, S_j(p.e.), versus the jet energy, is shown in fig. 18, for the various Xo cuts. The linearity is conserved in all cases. Straight lines in the plots correspond to linear fits to eq. (6). The slopes varied from 0.43

p.e./GeV, when no cut, to 0.35 p.e./GeV for 10 Xo cut. The fitted parameters, as a function of the Xo cut, are shown in fig. 19, while numerical values are displayed in table 1.

Using eq. (6), we have reconstructed the jet energy. Fig. 20 shows, for the various Xo cuts, the distributions of

$$R = (E_r - E_j)/E_j \qquad (8)$$

where, E_r is the reconstructed energy of a jet with energy E_j (GeV).

Full lines in the plots correspond to Gaussian fits to the distributions. Fitted mean values (<R>) are in all cases close to zero. The fitted widths (σ_j) are the average energy resolutions (<$\sigma(E_j)/E_j$> = σ_j) of the jets in the 11 geometrical scenarios considered. The numerical values are presented in Table 1.

<R>, as a function of the gamma content in a jet (five intervals are used), is shown in fig. 21 for the various cuts. We observe that for no light suppression (0 Xo cut), the higher is the gamma content in a jet, the higher is <R>. This positive correlation becomes smaller and smaller as we increase the Xo cut. The correlation vanishes in the 8 Xo cut region (*jet compensation*) and becomes negative for higher Xo cuts.

A similar effect is observed when plotting the collected signal (in p.e.) versus the gamma fraction in a jet (fig. 22). Again, compensation is observed in the region of 8 Xo cut.

The jet energy resolution is not affected by the cuts (for < 10 Xo). This is seen in fig. 23 and presented in Table 1. Moreover, the jet energy resolution has a minimum in the neighbouring of 8 Xo cut. We illustrate this point in fig. 24, where σ_j is plotted as a function of the Xo cut. If we compare these results with the expectations using a calorimeter having two sections fully equipped (eqs. (2) to (5)), the relative degradation of the jet energy resolution is smaller than 15% [14].

For completeness, we show (figs. 25 a) and b)) that the shapes of the jet transverse profiles are not affected by the Xo cut. The signal at the maximum is suppressed, in average, by $\approx$ 11%, while the signal from pileup background [15] decreases, in average, $\approx$ 28% (figs. 26 a) and b)). This will reinforce the capabilities for jet finding and reconstruction, as increasing the signal/noise ratio (figs. 27 a) and b)).

5. Summary and conclusions

In view of the design of a compensating quartz fiber calorimeter, single particles as well as tagging jets were fully simulated within a non-segmented quartz fiber calorimeter, which contained in its front an uninstrumented dummy "section" (0 Xo to 10 Xo).

The conclusions reached from a detailed Monte-Carlo analysis are as follows:

The level of compensation for single particles varied from 1.6 (undercompensation) with no cut to less than 1 (overcompensation) for 10 Xo cut. A reasonable level of compensation ($\approx$ 1.2) is found for $\approx$ 8 Xo cut. Also, we observe no significant degradation of the hadron energy resolution.

There exist a dummy section thickness ($\approx$ 8 Xo) such that the response for tagging jets is independent of their gamma content (compensation in jets), while keeping linearity of the response with respect to the jet energy. This Xo cut leads to a better jet energy resolution than the one obtained with no light suppression. Now, comparing this to a calorimeter having two equipped sections, the expected average degradation of the jet energy resolution is smaller than 15%.

We finally conclude that the above proposed solution would lead to a compact, compensating and low cost VFCAL quartz fiber calorimeter satisfying the required physics performance.

Acknowledgements

References

[1] "CMS Technical Proposal", CERN LHCC 94-38 (1994).
[2] A. Contin et al., "R&D Proposal for development of quartz fiber calorimetry", CERN DRDC/94-4 (1994).
[3] G. Anzivino et al., Nucl. Instr. and Methods A 357 (1995) 380.
[4] P. Gorodetzky et al., Nucl. Instr. and Methods A 361 (1995) 161.
[5] R. Wigmans, Nucl. Instr. and Methods A 259 (1987) 389.
[6] R. Wigmans, Nucl. Instr. and Methods A 265 (1988) 273.
[7] C. W. Fabjan and R. Wigmans, Rep. Prog. Phys. 52 (1989) 1519.
[8] C. Bacci et al., Nucl. Instr. and Methods A 292 (1990) 113.
[9] M.C. Fouz et al., "R&D Proposal: Very forward calorimetry at the LHC using parallel plate chambers", CERN/DRDC 93-43 (1993).
[10] Gy. L. Bencze et al., CMS Technical Note TN/96-075 (1996).
[11] J. V. Jelley, "Cherenkov radiation and its applications", Pergamon Press, 1958.
[12] R. Brun et al., CERN DD/EE/84-1 (1987). See also CERN Program Library Writeup W5023 (1993).
[13] A. Ferrando et al., CMS Technical Note TN/95-038 (1995).
[14] Yu. Gershtein, private communication.
[15] C. Burgos et al., CMS Technical Note TN/95-035 (1995).

Table captions

Table 1: Results from the fits (see text) to: linearity of the response, energy reconstruction and energy resolution, for the tagging jet sample.

X0 cut	S(p.e.) = $\alpha \times E(\text{GeV}) + \beta$		$R = \frac{E_r - E_j}{E_r}$		$\frac{\sigma(E_j)}{E_j} = \frac{a}{\sqrt{E_j}} + b$	
	α (p.e./GeV)	β (p.e.)	$<R>$	σ	a	b
0 X0	0.431±0.003	-3.67±3.86	0.007±0.003	0.098±0.002	2.19±0.46	0.03±0.01
1 X0	0.431±0.003	-3.84±3.86	0.007±0.003	0.099±0.002	2.30±0.47	0.03±0.01
2 X0	0.431±0.003	-4.37±3.86	0.007±0.003	0.099±0.002	2.29±0.47	0.03±0.01
3 X0	0.429±0.003	-5.80±3.83	0.007±0.003	0.097±0.002	2.01±0.47	0.04±0.01
4 X0	0.427±0.003	-8.64±3.78	0.006±0.003	0.094±0.002	2.03±0.48	0.03±0.01
5 X0	0.421±0.003	-12.30±3.65	0.007±0.003	0.092±0.002	1.58±0.50	0.05±0.02
6 X0	0.413±0.003	-17.33±3.45	0.007±0.003	0.087±0.002	1.77±0.40	0.03±0.01
7 X0	0.401±0.003	-22.39±3.14	0.004±0.002	0.082±0.002	1.28±0.32	0.04±0.01
8 X0	0.386±0.003	-27.65±2.94	0.007±0.002	0.082±0.002	1.86±0.37	0.03±0.01
9 X0	0.369±0.003	-31.36±2.90	0.004±0.003	0.090±0.002	1.97±0.37	0.03±0.01
10 X0	0.351±0.003	-33.49±2.94	0.007±0.003	0.105±0.003	2.76±0.49	0.02±0.01

Table 1

Figure captions

Fig. 1: The Cerenkov working principle in fibers.

Fig. 2: Sketch of the calorimeter module geometry used in the simulation.

Fig. 3: Average longitudinal shower profile, in the Cerenkov mode of operation and with copper as absorber material, for electrons (continuous line) and pions (dashed line), for:

    a) 100 GeV particles

    b) 500 GeV particles

Fig. 4: Distribution of the expected collected light in electron showers, for four different geometrical configurations (0 Xo, 4 Xo, 8 Xo and 10 Xo), for:

    a) 100 GeV

    b) 350 GeV

Fig. 5: Distribution of the expected collected light in pion showers, for four different geometrical configurations (0 Xo, 4 Xo, 8 Xo and 10 Xo), for:

    a) 100 GeV

    b) 350 GeV

Fig. 6: C_p as a function of the particle energy for the various Xo cuts (see text).

Fig. 7: $<C_p>$, in the range 200 GeV - 500 GeV, as a function of the Xo cut.

Fig. 8: Expected average value of the collected signal from electron showers, S_e (p.e.), as a function of the electron energy, for the various geometrical configurations considered in the text.

Fig. 9: Expected average value of the collected signal from pion showers, S_π (p.e.), as a function of the pion energy, for the various geometrical configurations considered in the text.

Fig. 10: Slope (α) and constant term (β) from fits to the linearity plots (see text) for electron showers, as a function of Xo cut.

Fig. 11: Slope (α) and constant term (β) from fits to the linearity plots (see text) for pion showers, as a function of Xo cut.

Fig. 12: Electron energy resolution as a function of the particle energy for the various Xo cuts.

Fig. 13: Pion energy resolution as a function of the particle energy for the various Xo cuts.

Fig. 14: Fitted values for the energy resolution parameters (see text) as a function of the particle energy, for:

    a) electrons

    b) pions

Full circles represent the stochastic term. Open circles correspond to the constant term.

Fig. 15: Energy resolution for 100 GeV (full circles) and 500 GeV (open circles) particles as a function of the Xo cut, for:

a) electrons

b) pions

Fig. 16: From the tagging jets sample (see text):

a) jet energy distribution

b) distribution of the γ fraction in jets

Fig. 17: From the tagging jet sample (see text):

a) average value of the γ fraction in jets as a function of the jet energy

b) average value of the jet energy as a function of the γ fraction in jets.

Fig. 18: Expected average value of the collected signal from jet showers, S_j (p.e.), as a function of the jet energy, for the various geometrical configurations considered in the text.

Fig. 19: Slope (α) and constant term (β) from fits to the linearity plots (see text) for jet showers, as a function of Xo cut.

Fig. 20: $R = (E_r - E_j)/E_j$ distribution, for the various Xo cut.

Fig. 21: $\langle R \rangle$ as a function of the γ fraction in jets, for the various Xo cuts.

Fig. 22: Average value of the collected signal for jets, S_j (p.e.), as a function of the γ fraction in jets, for various Xo cut.

Fig. 23: Jet energy resolution (see text), as a function of the jet energy, for the various Xo cuts.

Fig. 24: Mean value of the jet energy resolution, for the whole tagging jet sample, as a function of the Xo cut.

Fig. 25: Average transverse profile of a tagging jet. Each square in the lego plot represents an area of 5 x 5 cm2. Size of the signal is given in p.e. (normalized to one event), for:

a) no Xo cut

b) 8 Xo cut

Note: The center of gravity of the jets has been translated to the center of the calorimeter module, regardeless of their actual position on VFCAL.

Fig. 26: Average transverse profile for pile-up background (see text) from one bunch crossing ($\approx$ 25 pp collisions):

a) no Xo cut

b) 8 Xo cut

Fig. 27: Random association of one jet and one underlying bunch crossing:

a) no Xo cut

b) 8 Xo cut

cerenkov cone

particle

z axis

numerical
aperture cone

Figure 1

Beam

x

z

y

15 cm

135 cm

15 cm

PM

mirrors fiber
end

bundle

beam
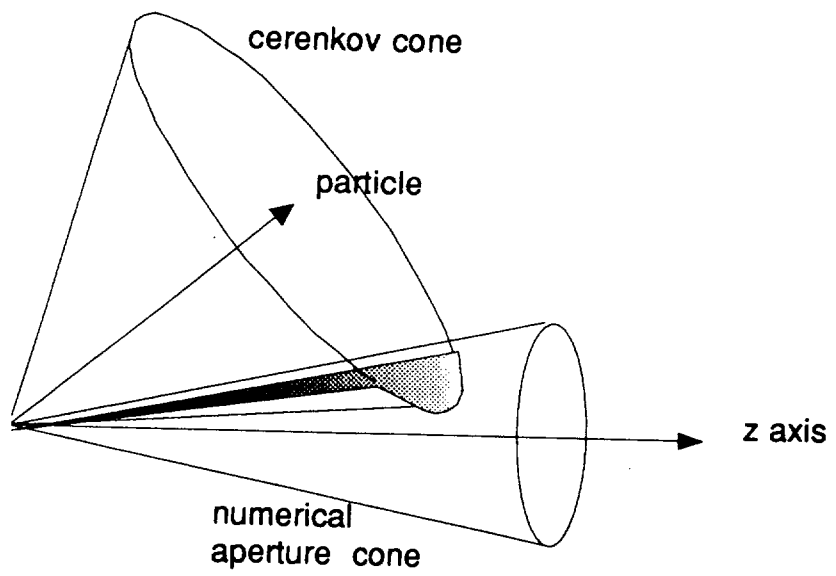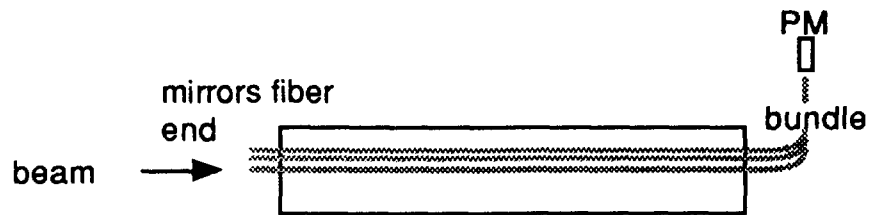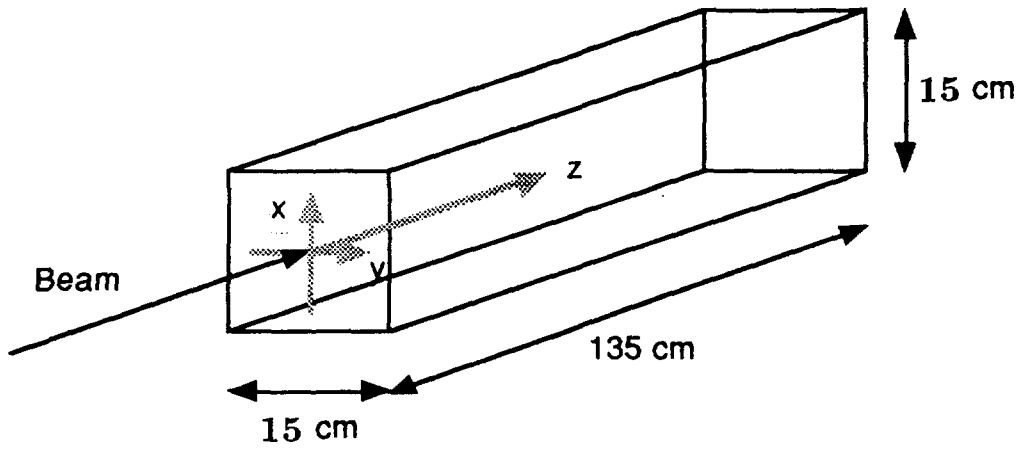
Figure 2

Longitudinal profiles
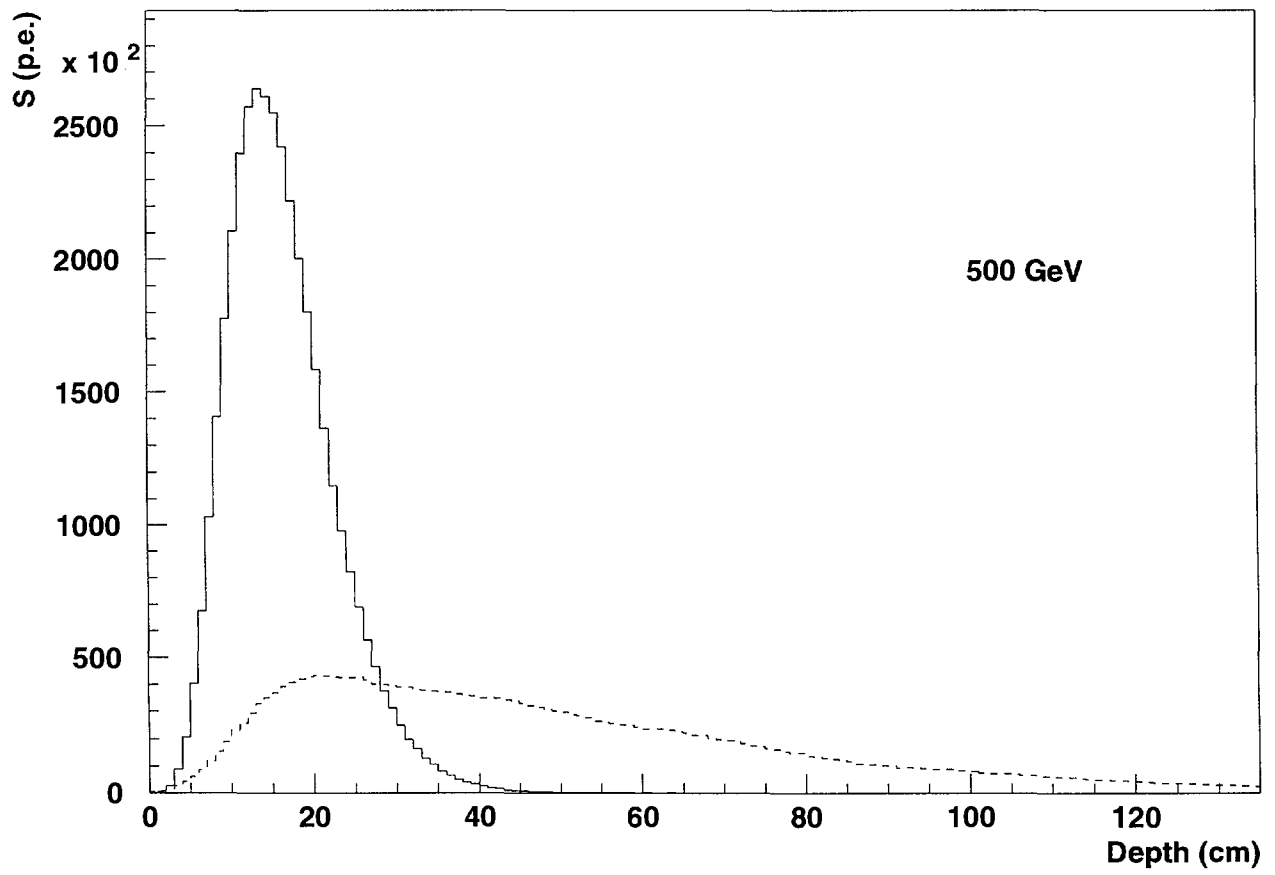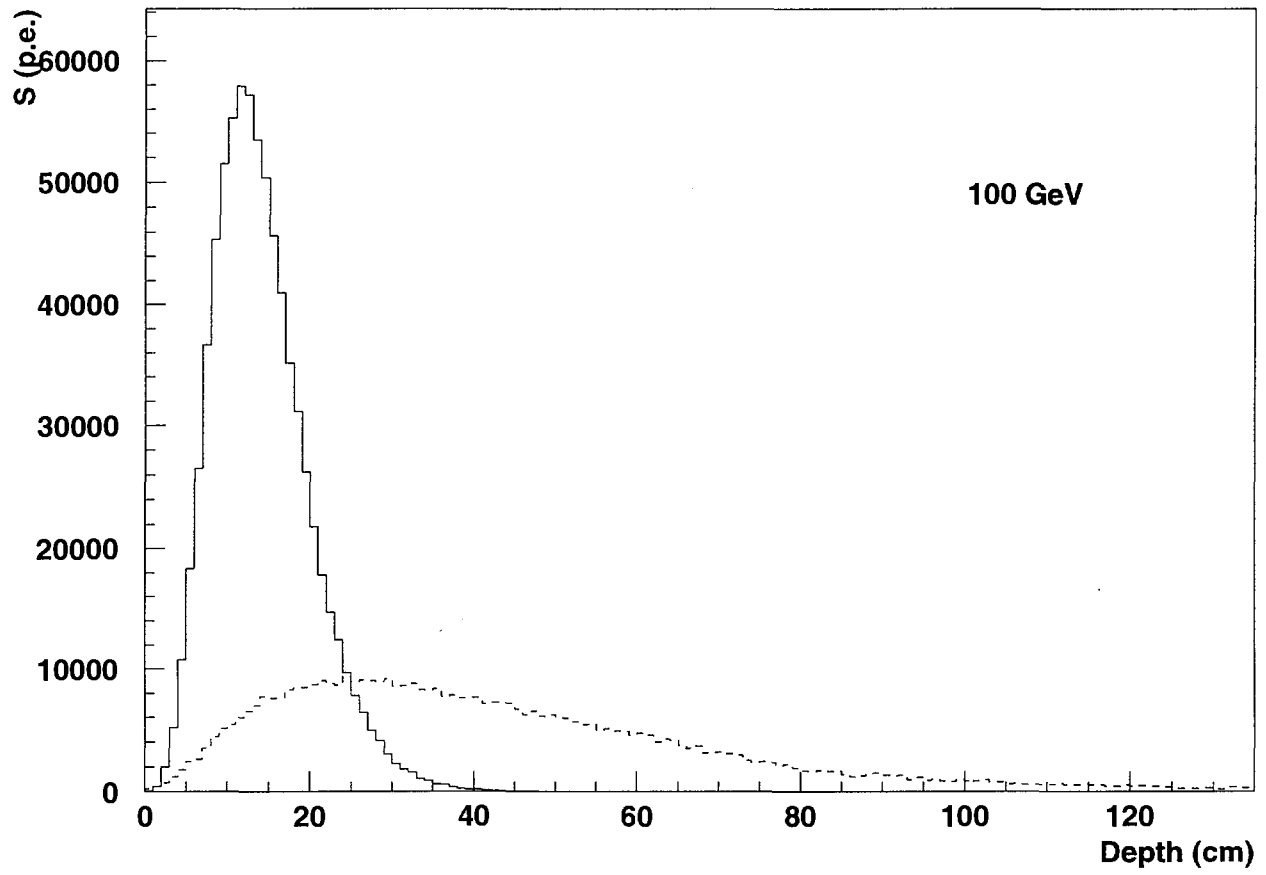
Figure 3

100 GeV electrons
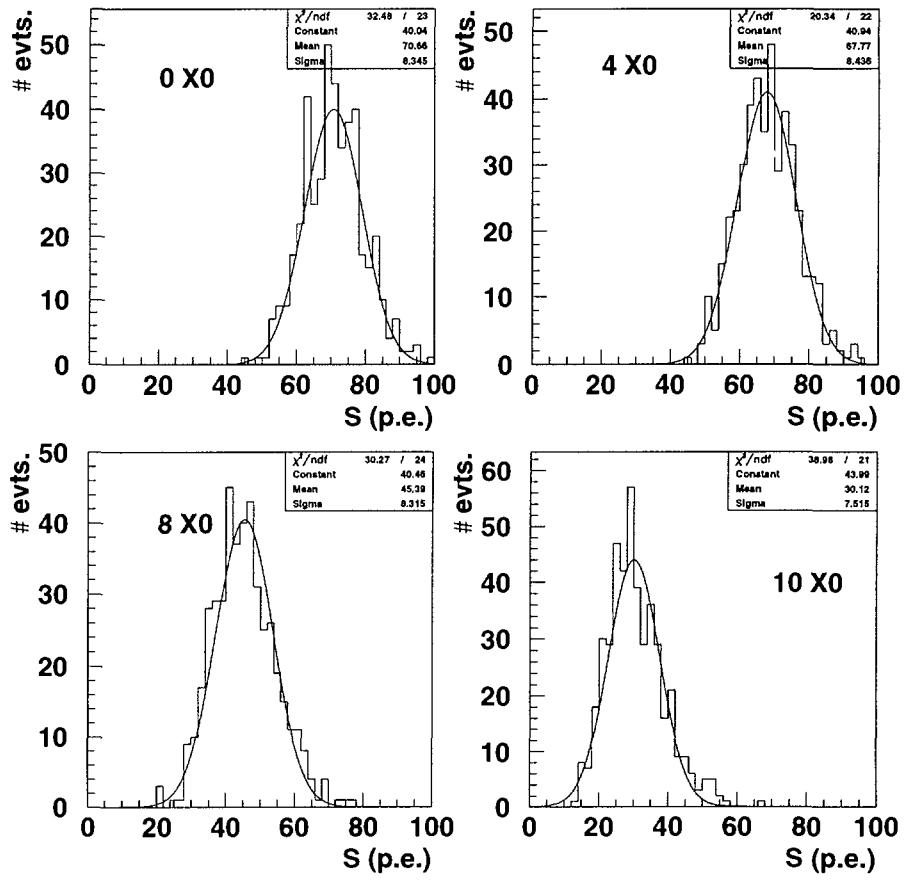
350 GeV electrons
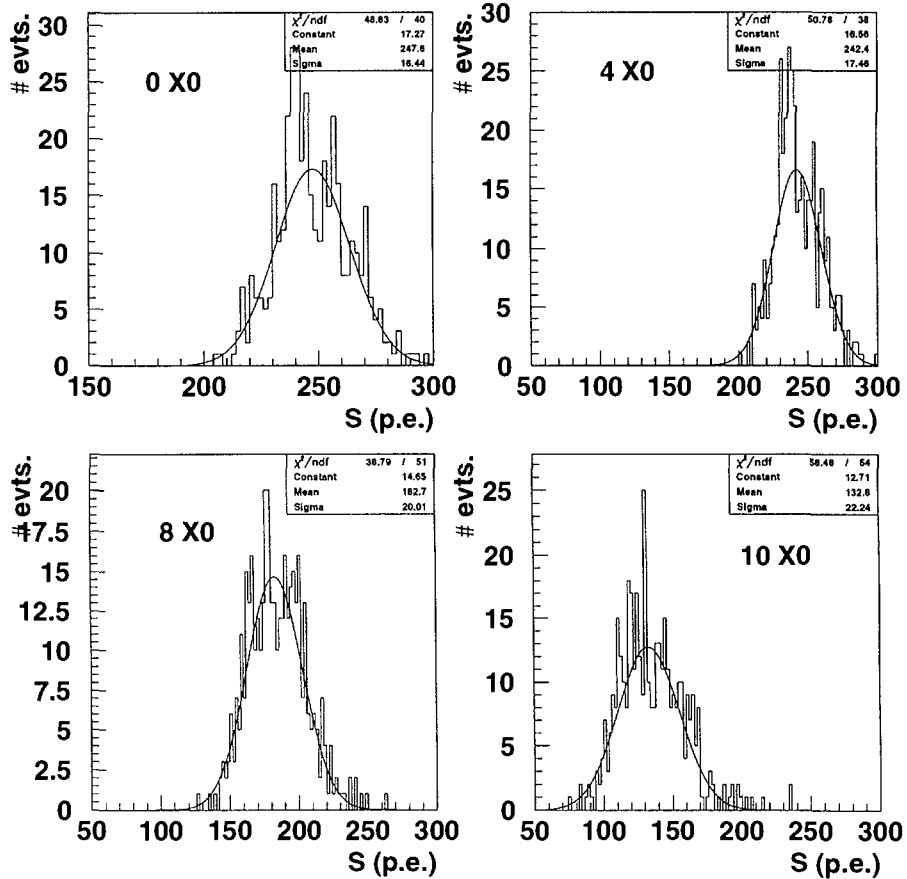
Figure 4

100 GeV pions
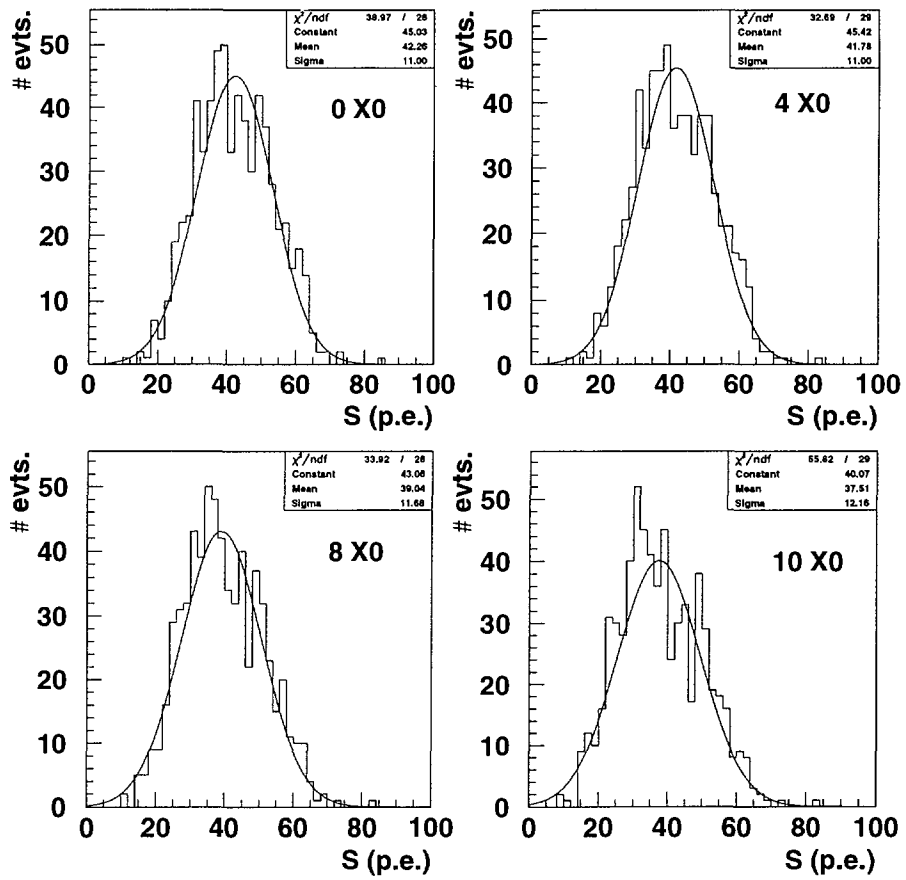
350 GeV pions
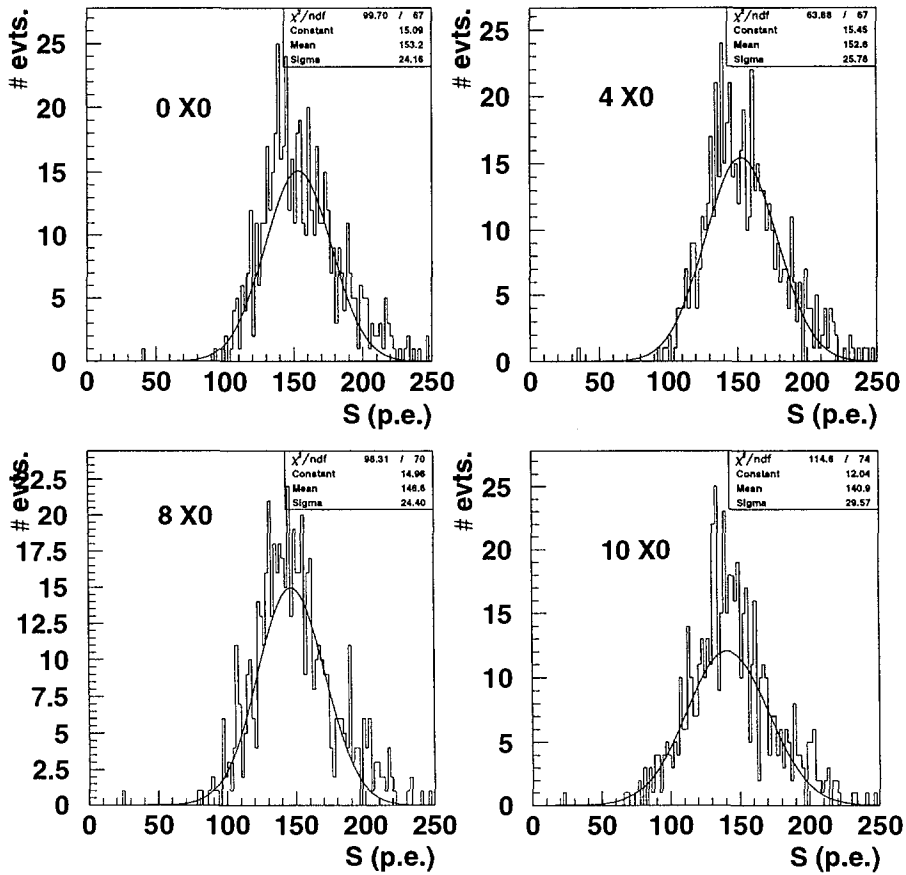
Figure 5

Compensation
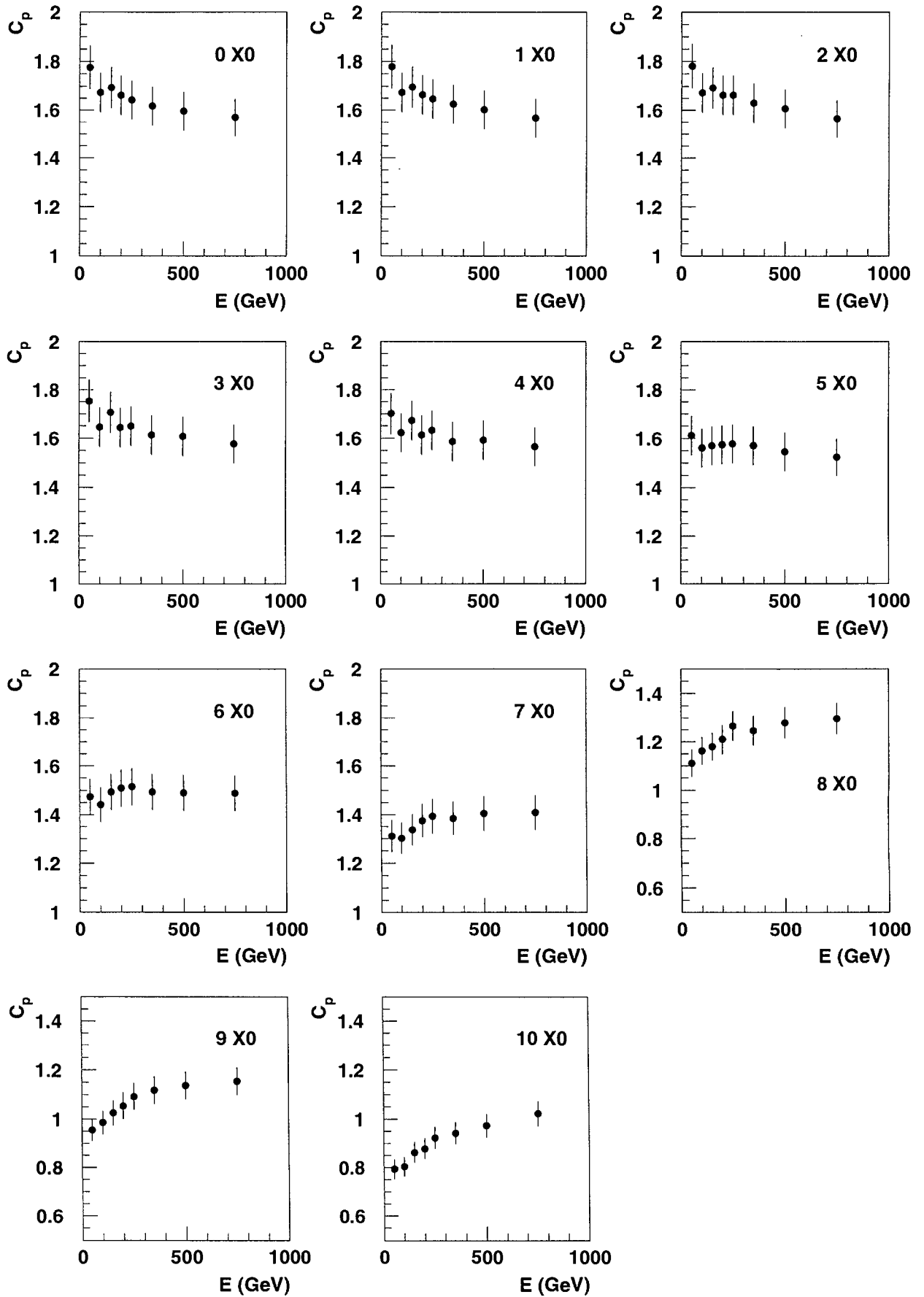
Figure 6
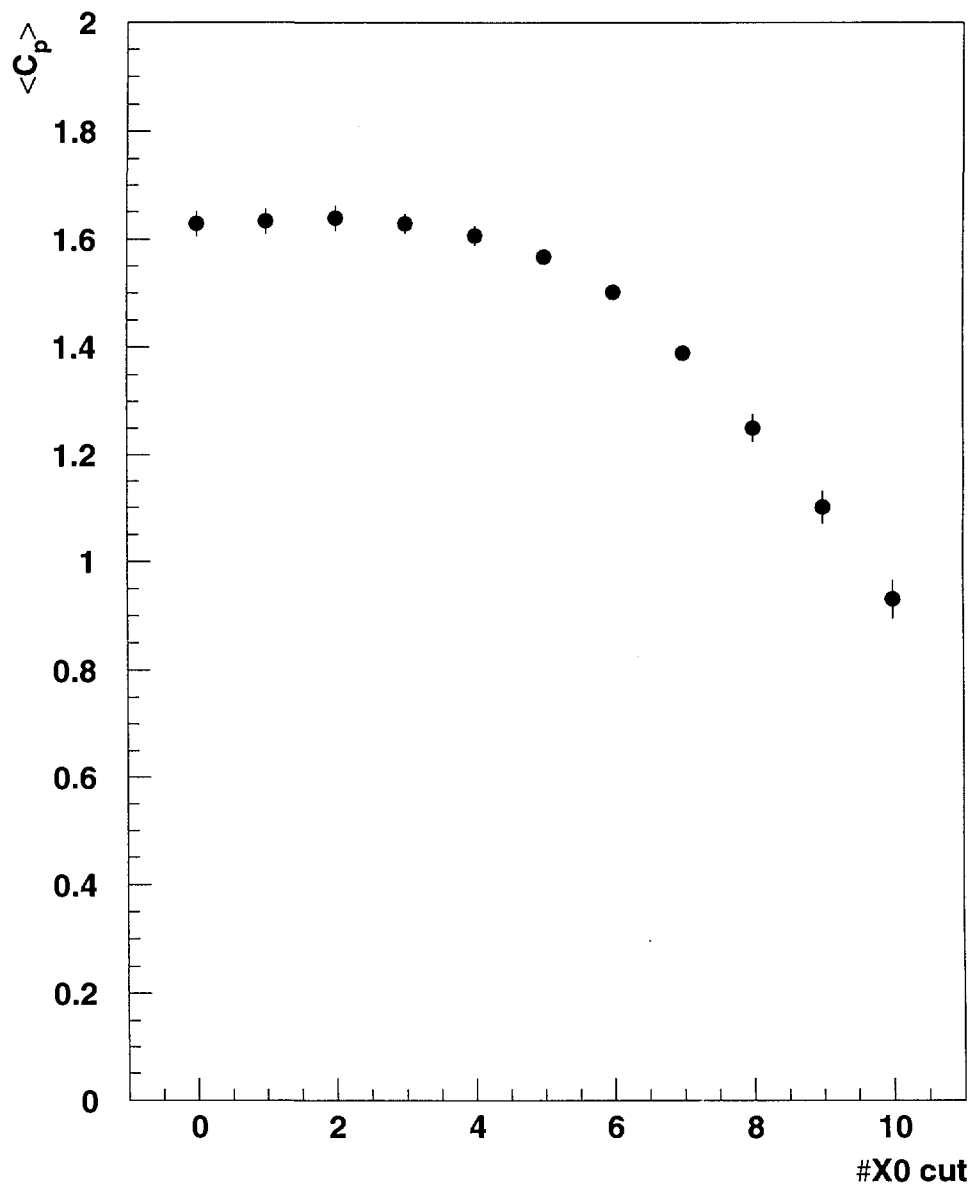
Figure 7

Linearity electrons
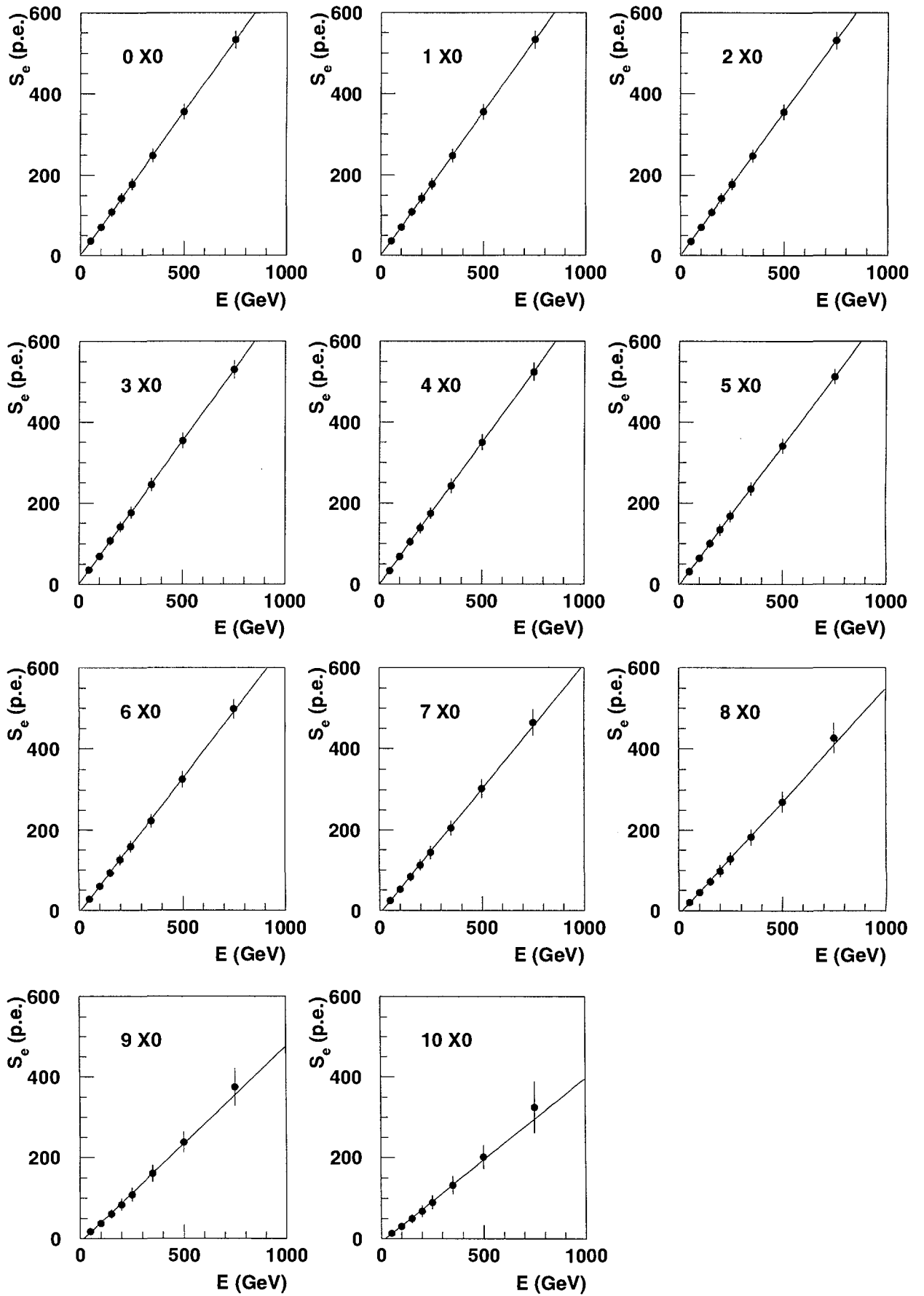
Figure 8

Linearity pions
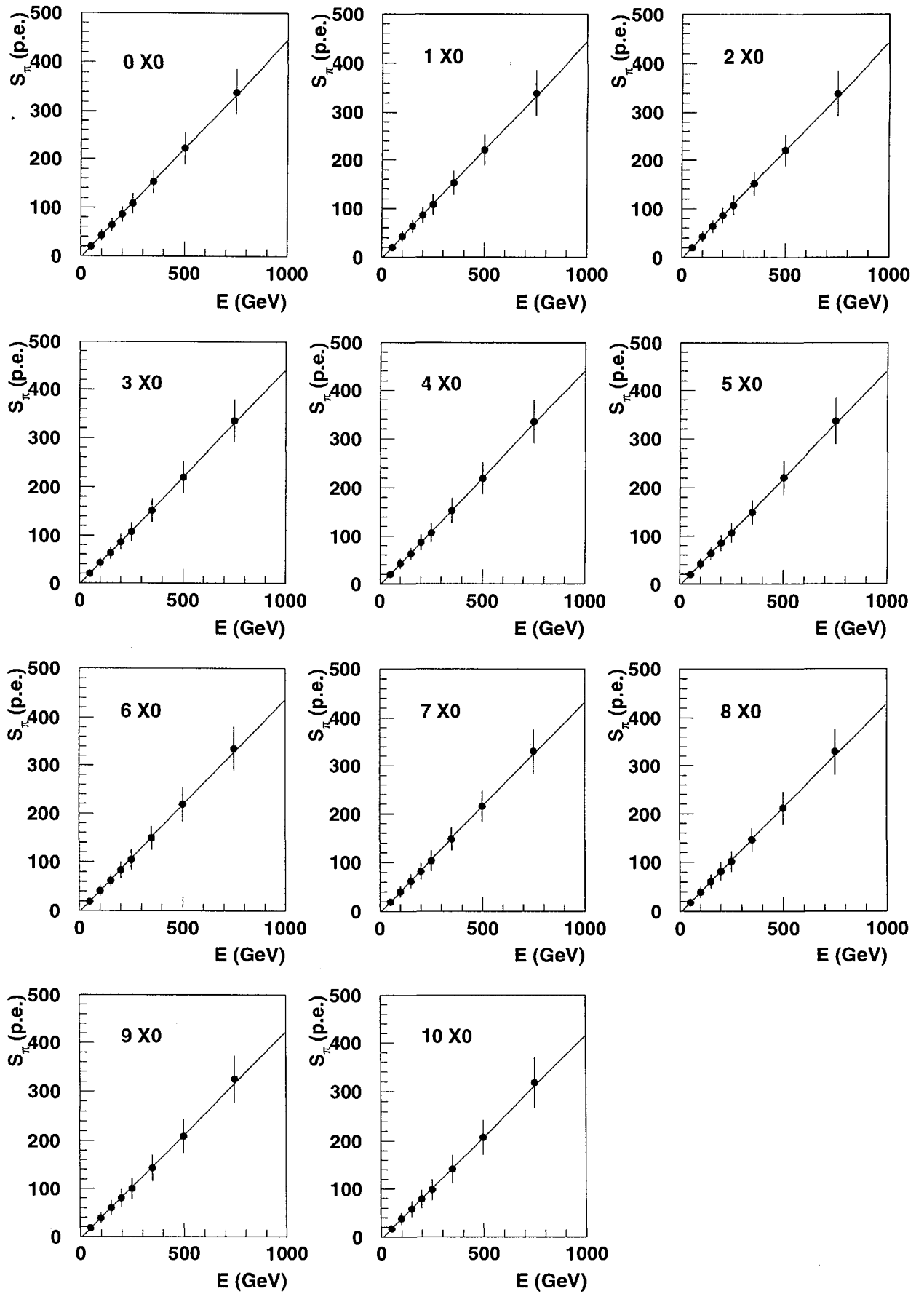
Figure 9

Electron linearity parameters vs X0 cut
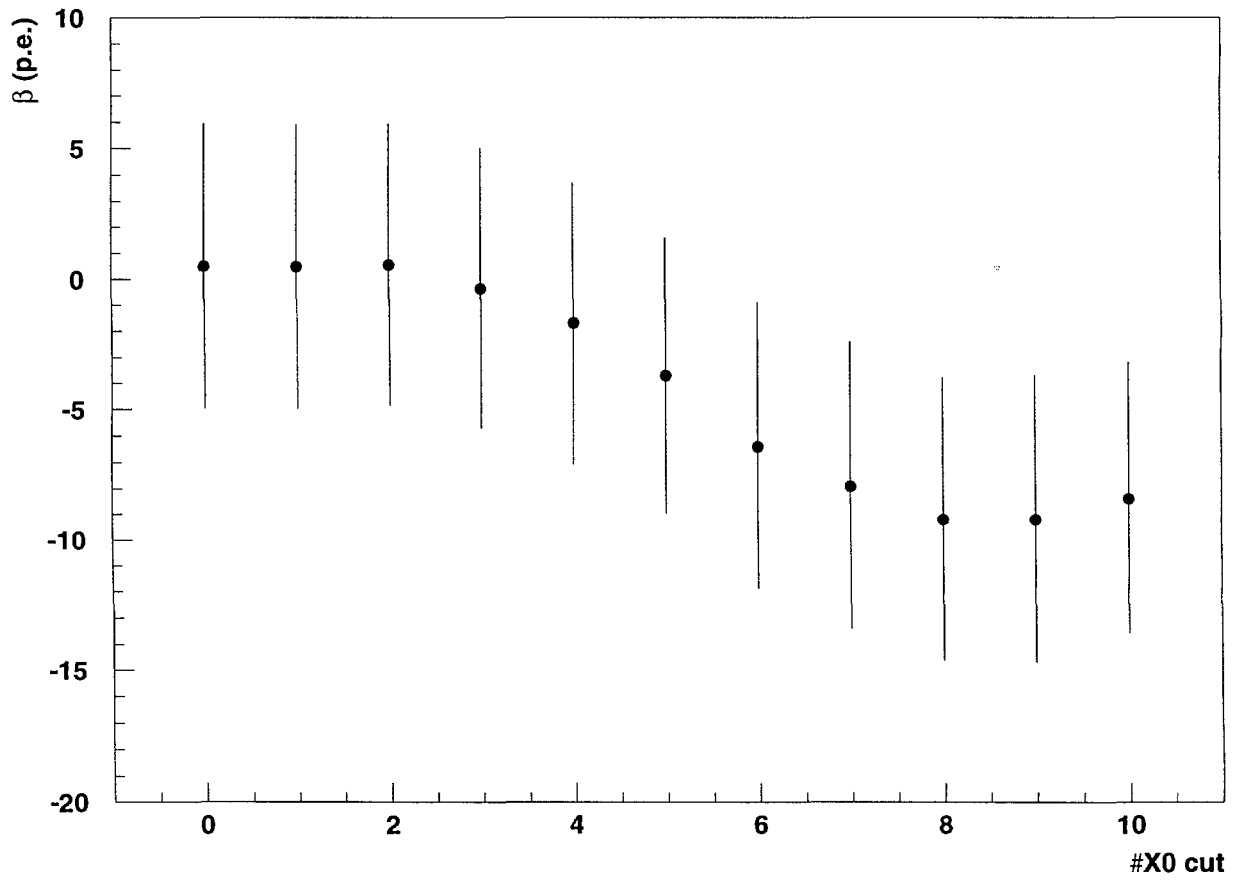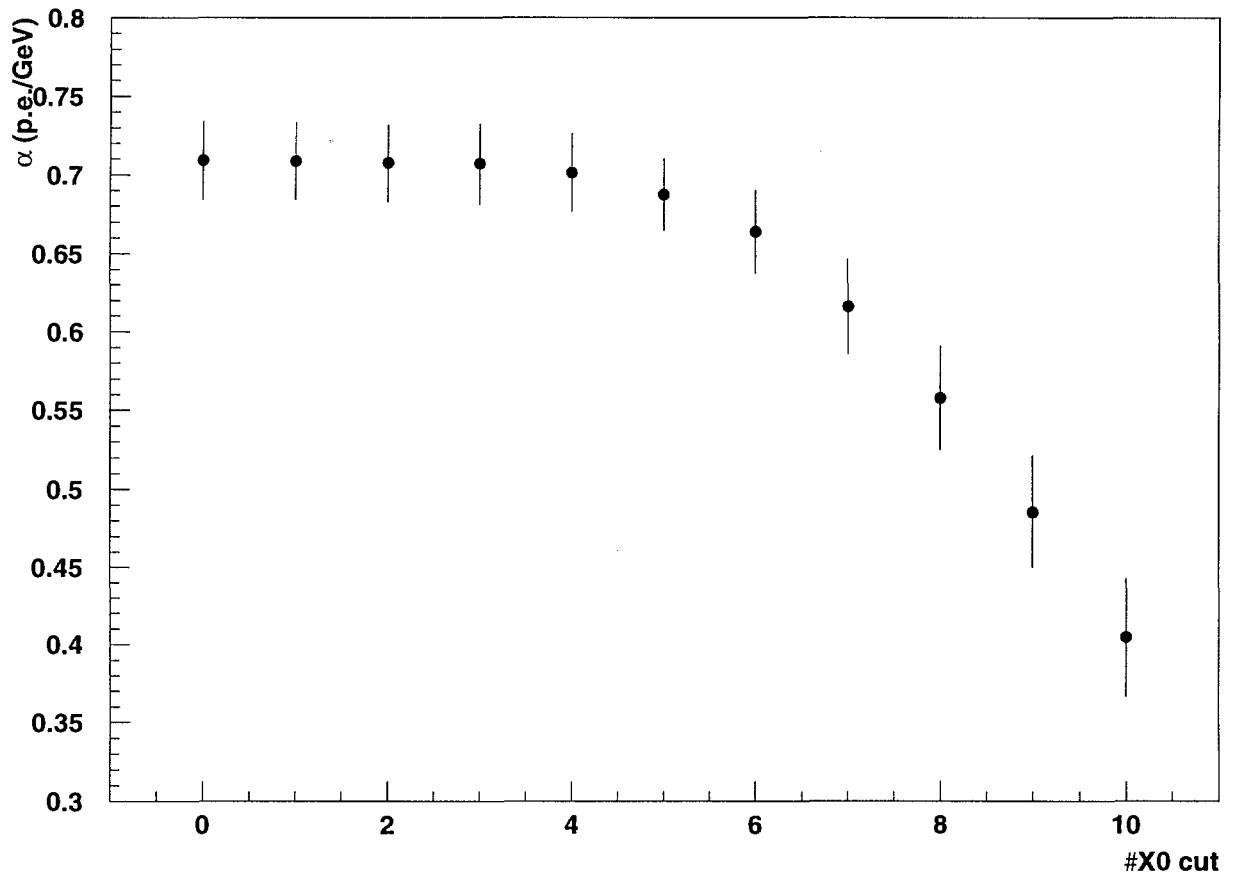
Figure 10

Pion linearity parameters vs X0 cut
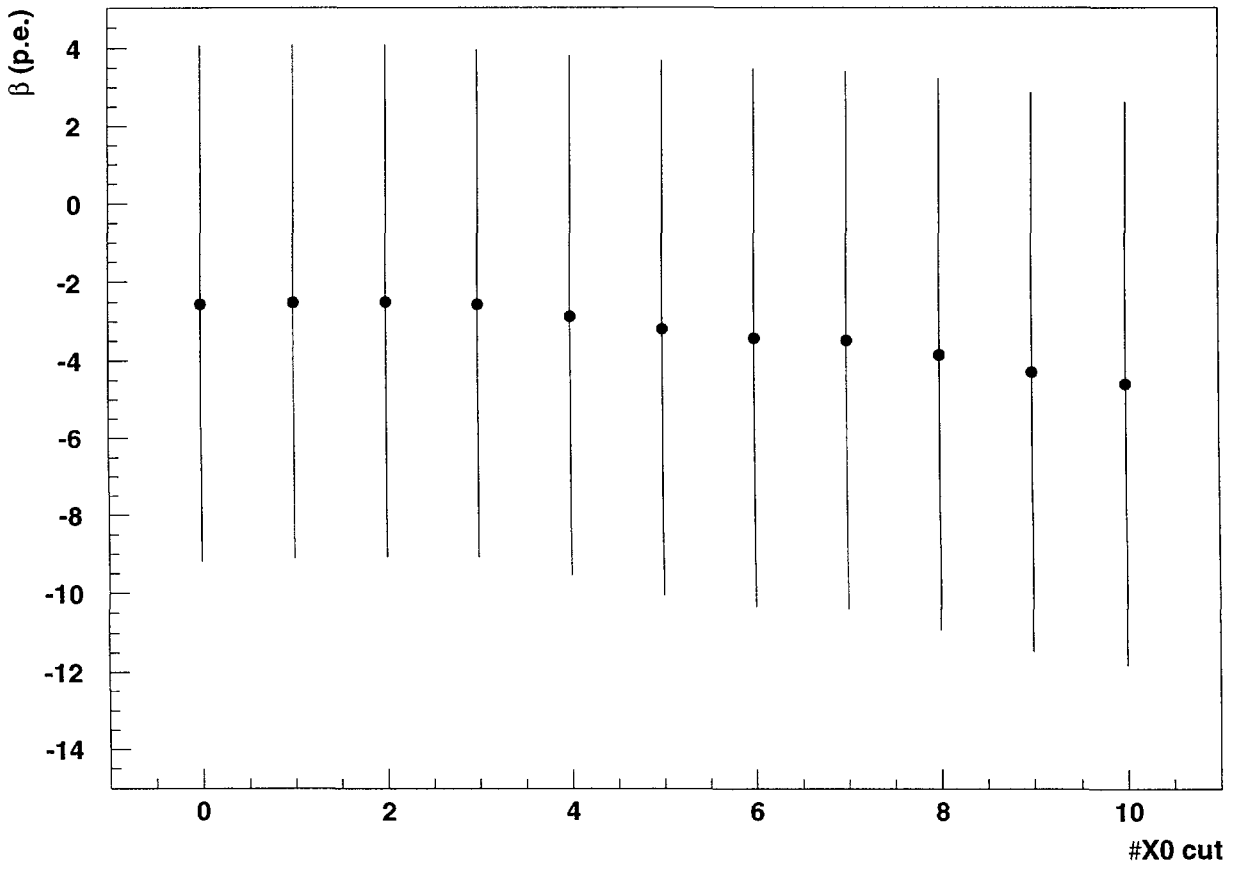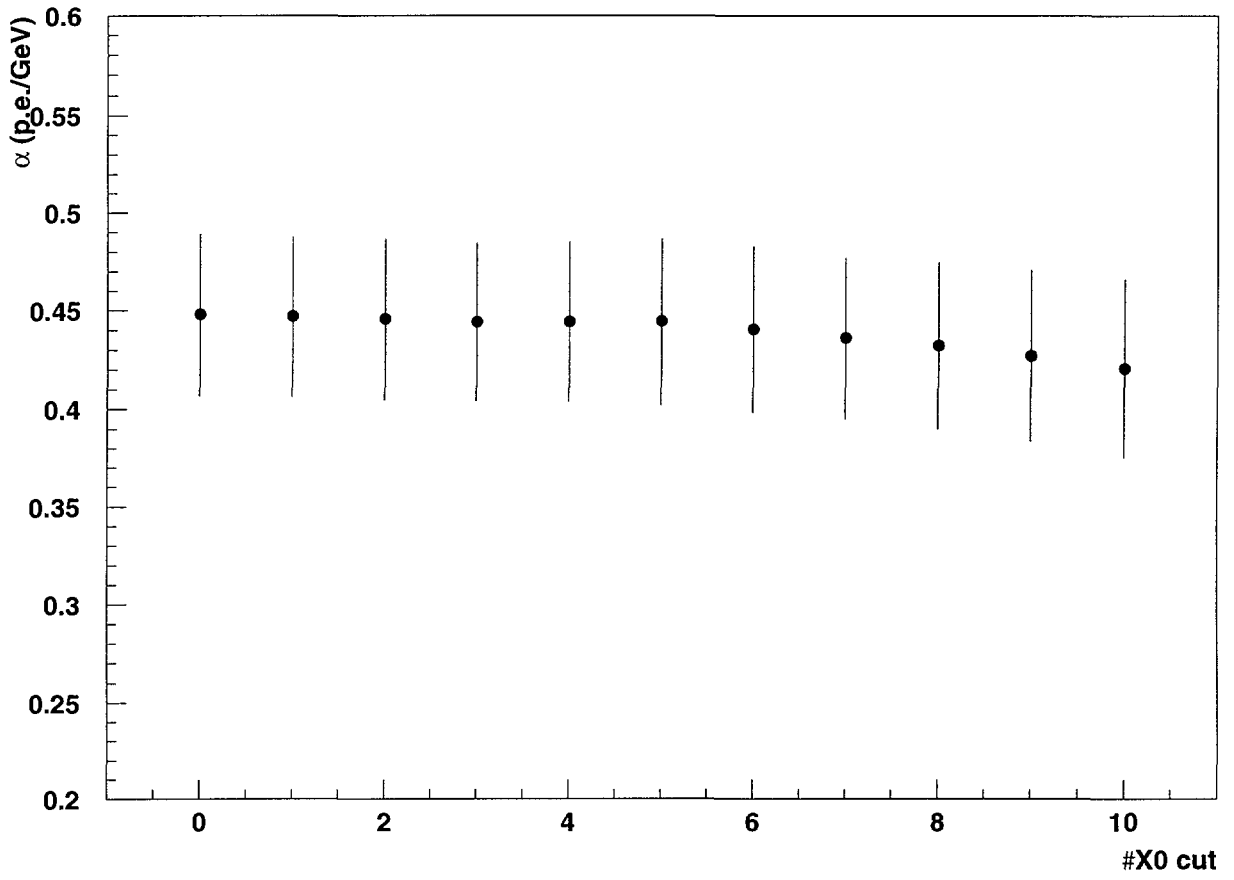
Figure 11

Electron energy resolution
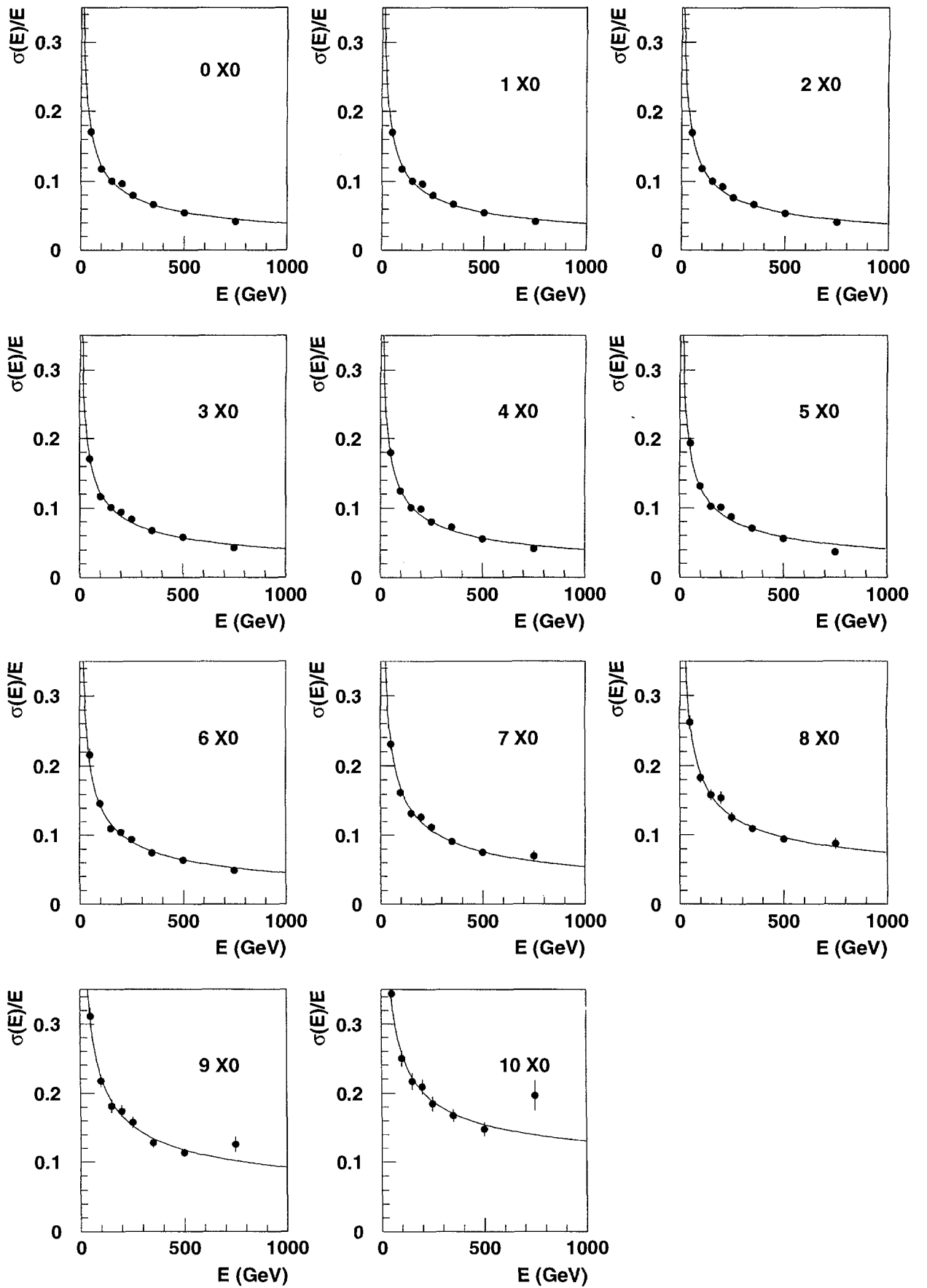
Figure 12

Pion energy resolution
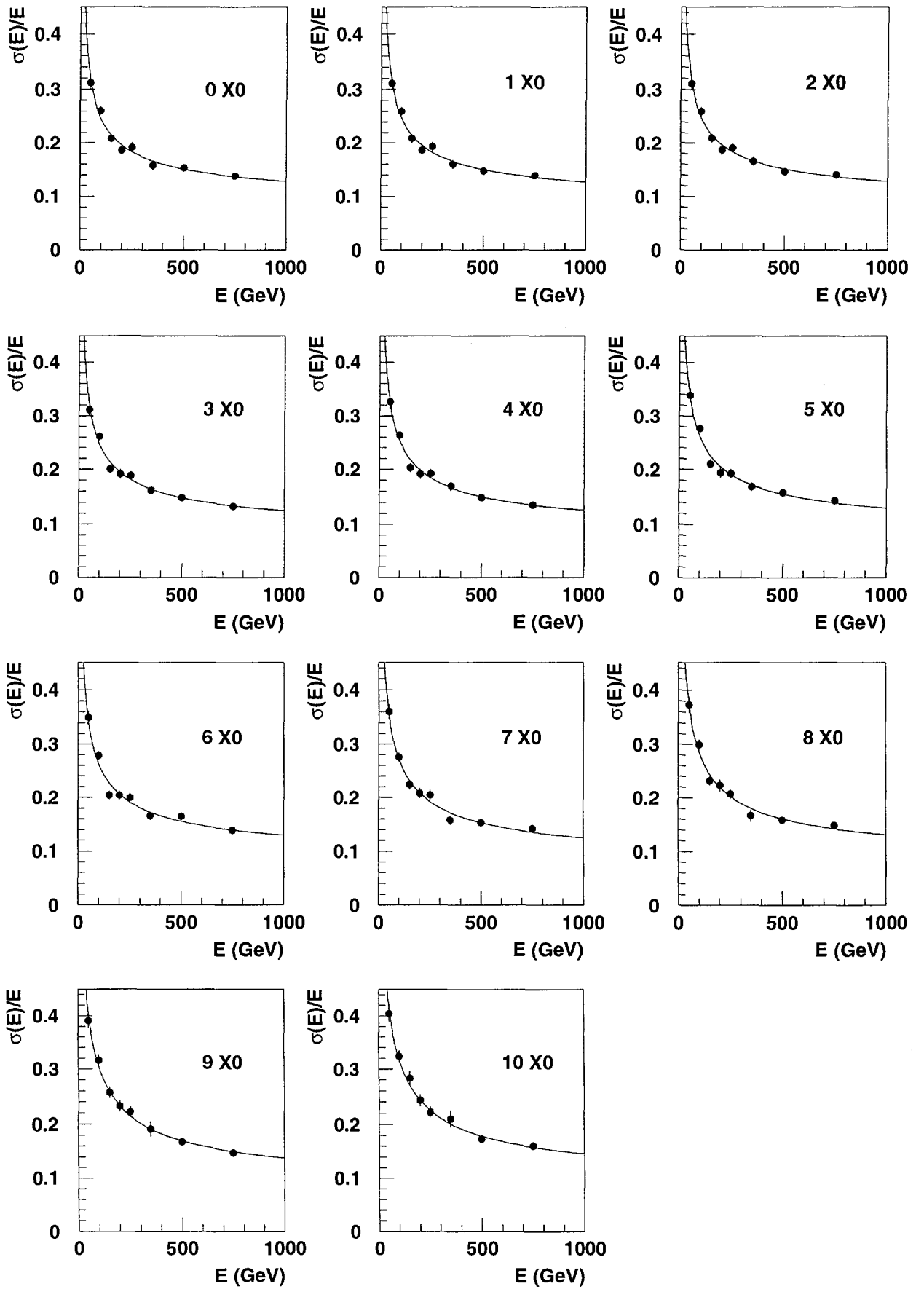
Figure 13

Electron energy resolution parameters vs X0 cut
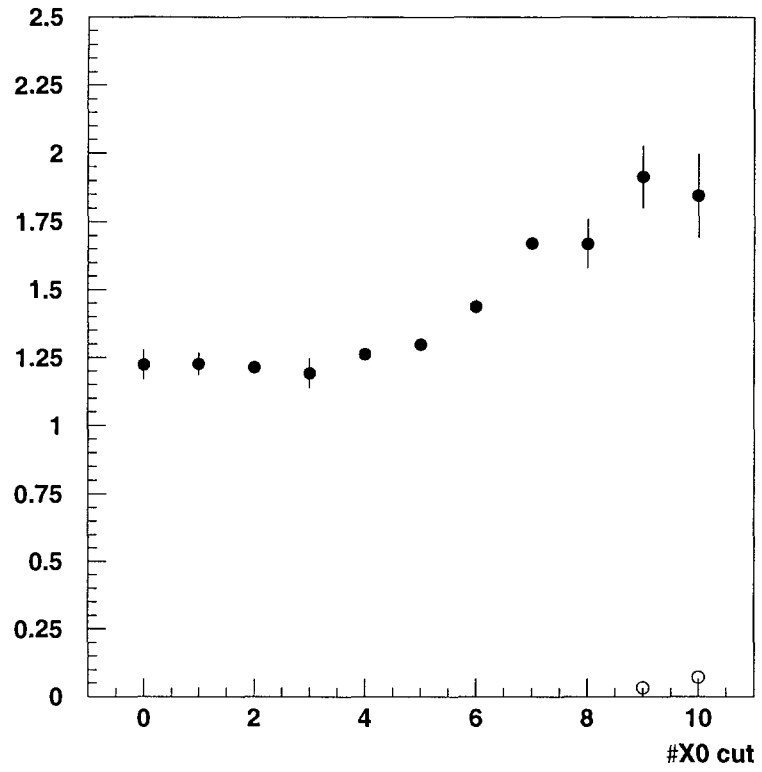
Pion energy resolution parameters vs X0 cut
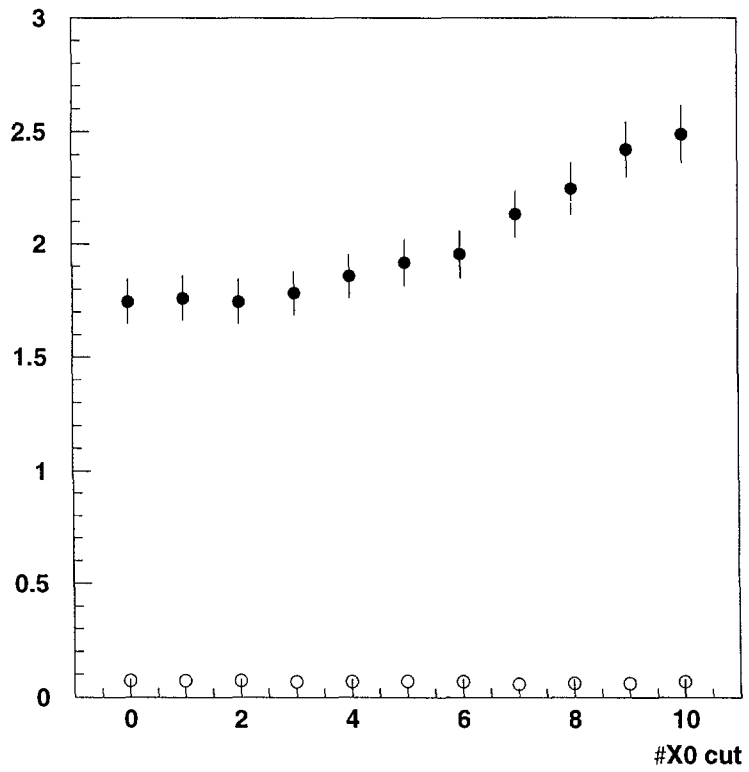
Figure 14
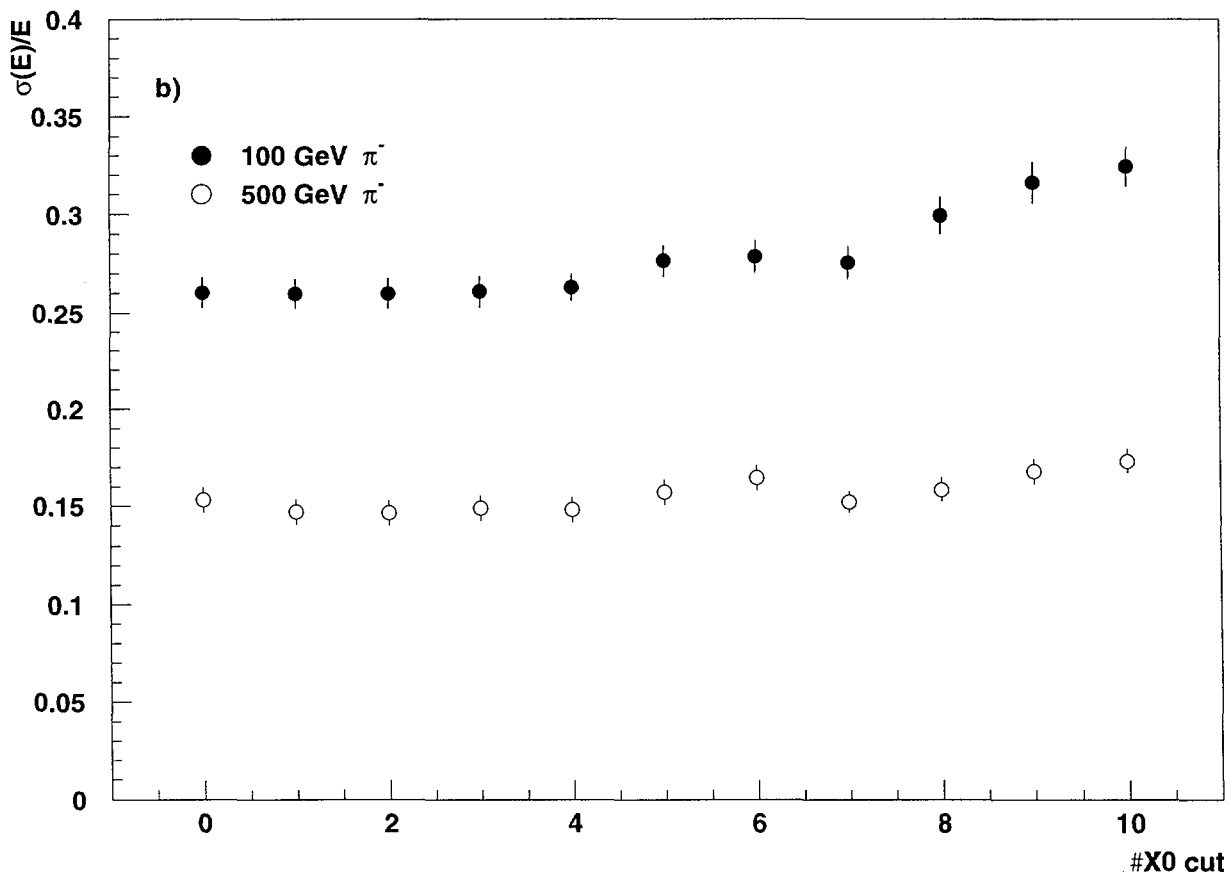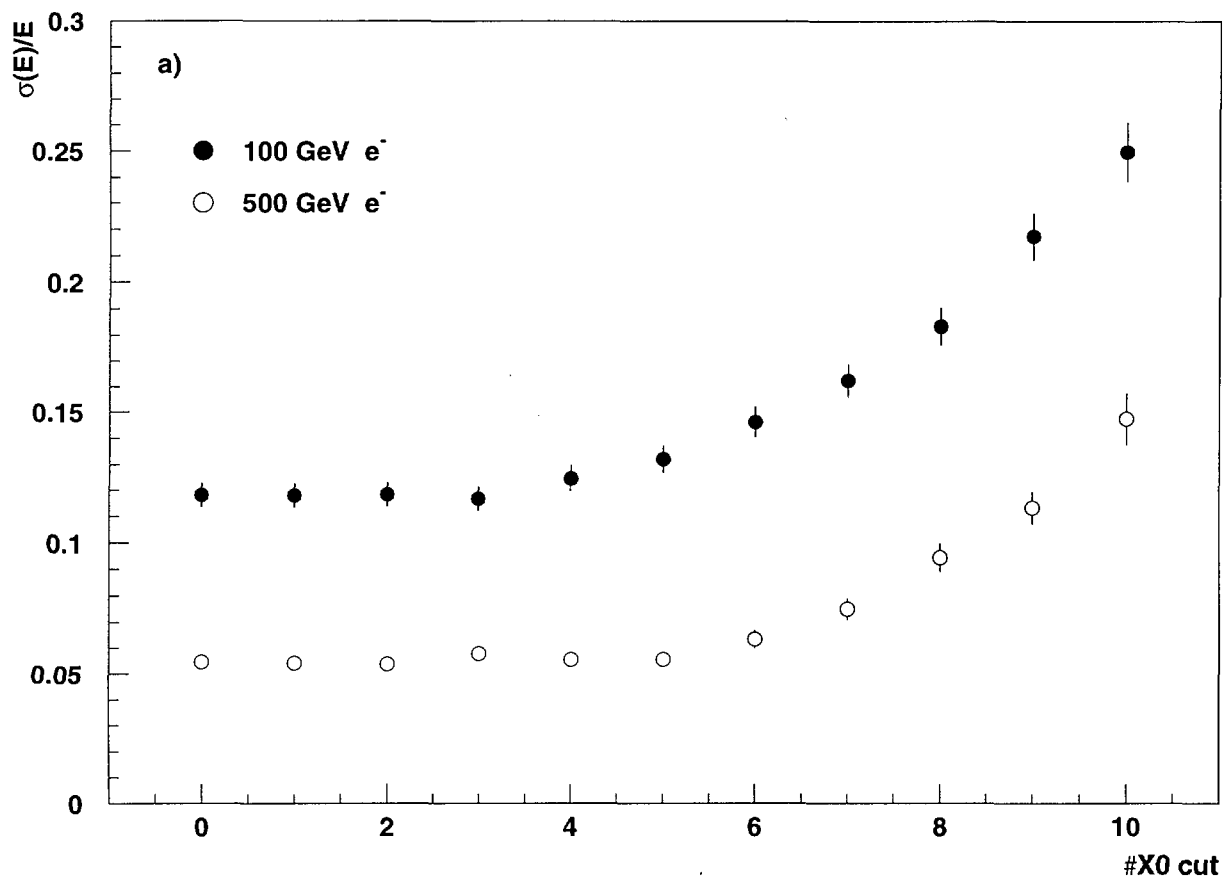
Figure 15
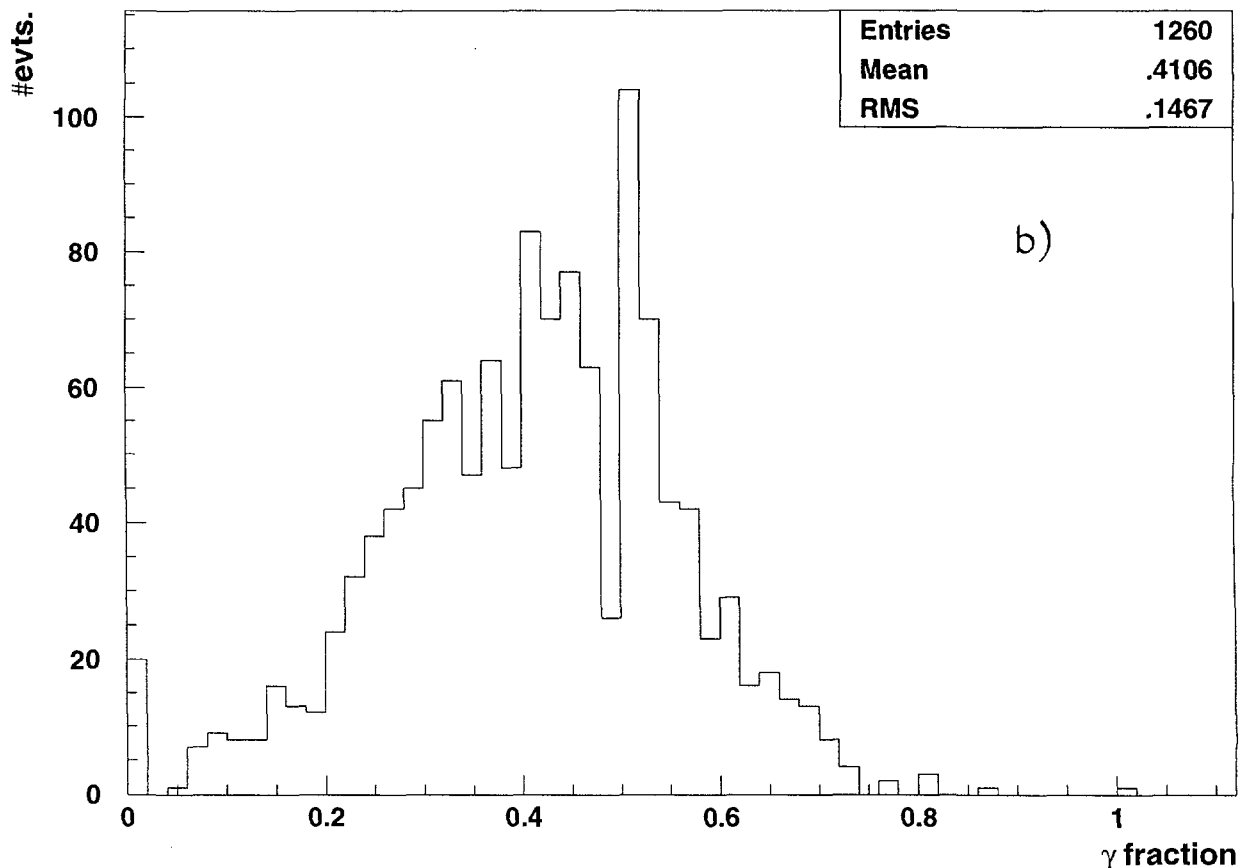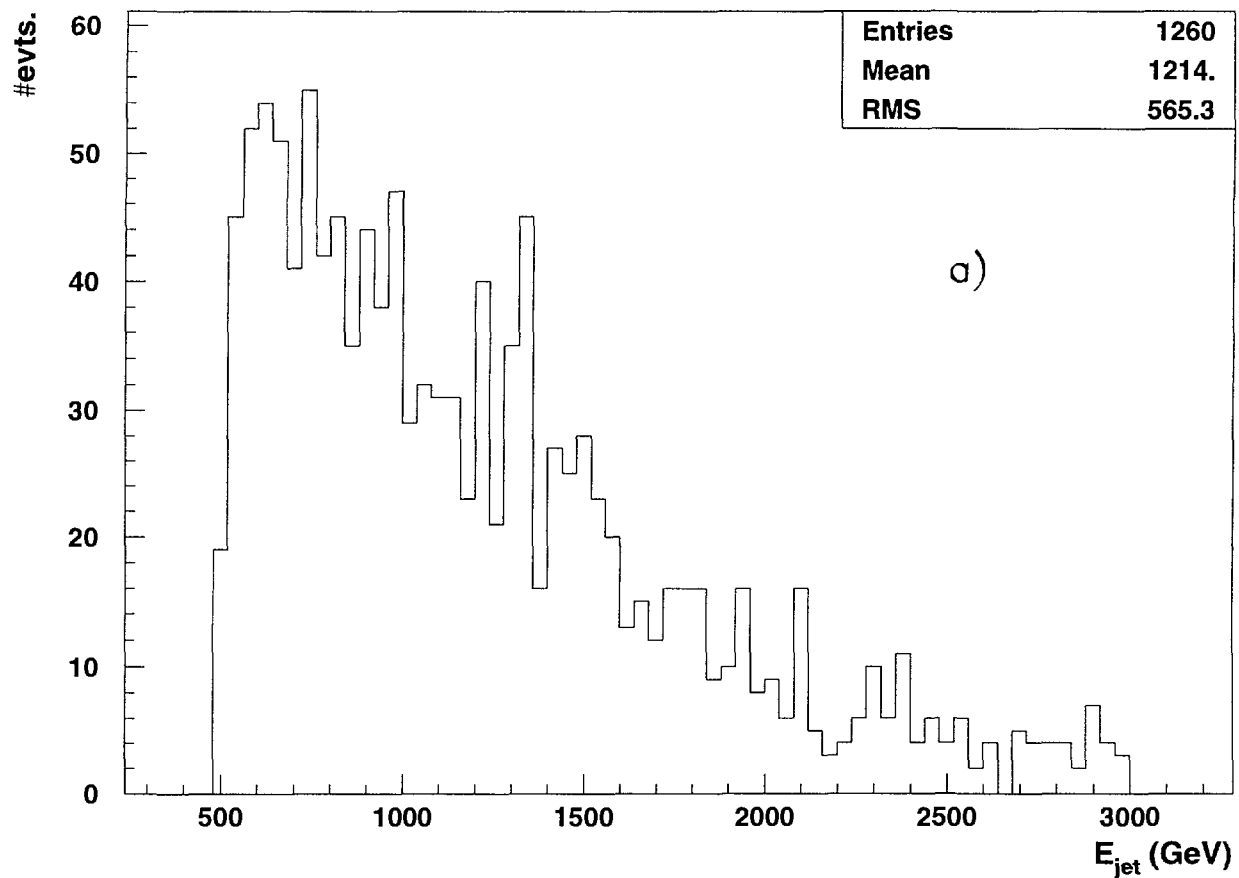
Figure 16
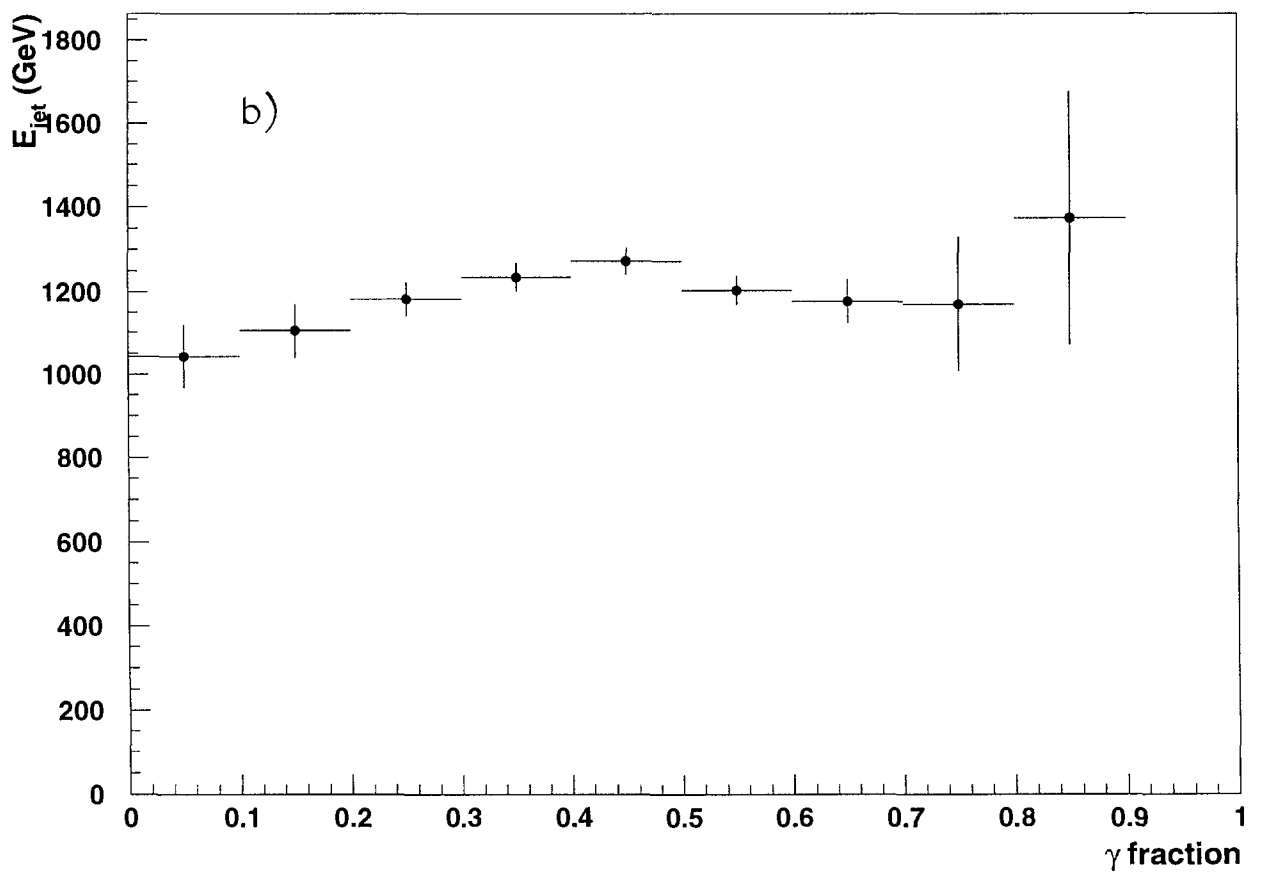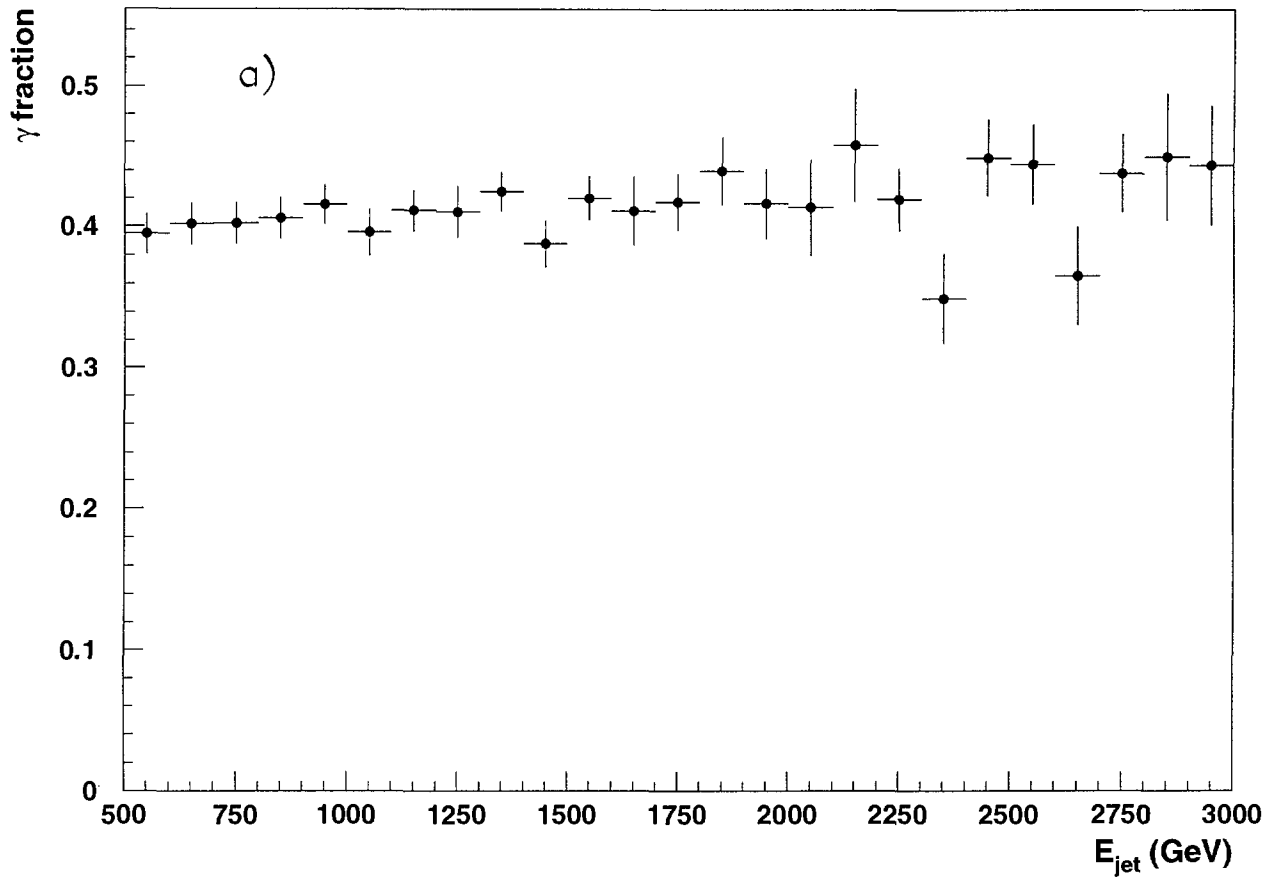
Figure 17

Expected collected light vs jet energy
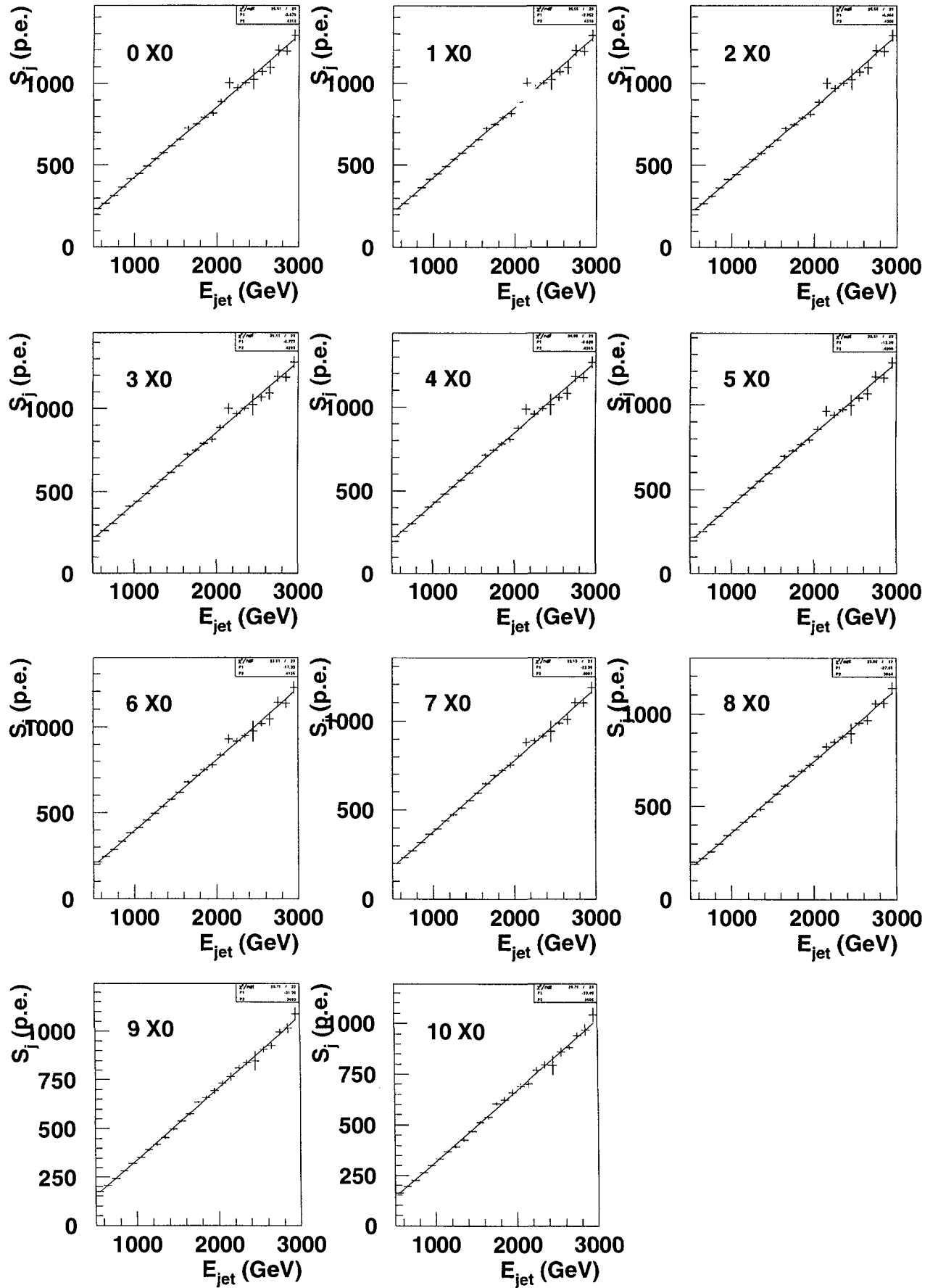
Figure 18

Jet linearity parameters vs X0 cut
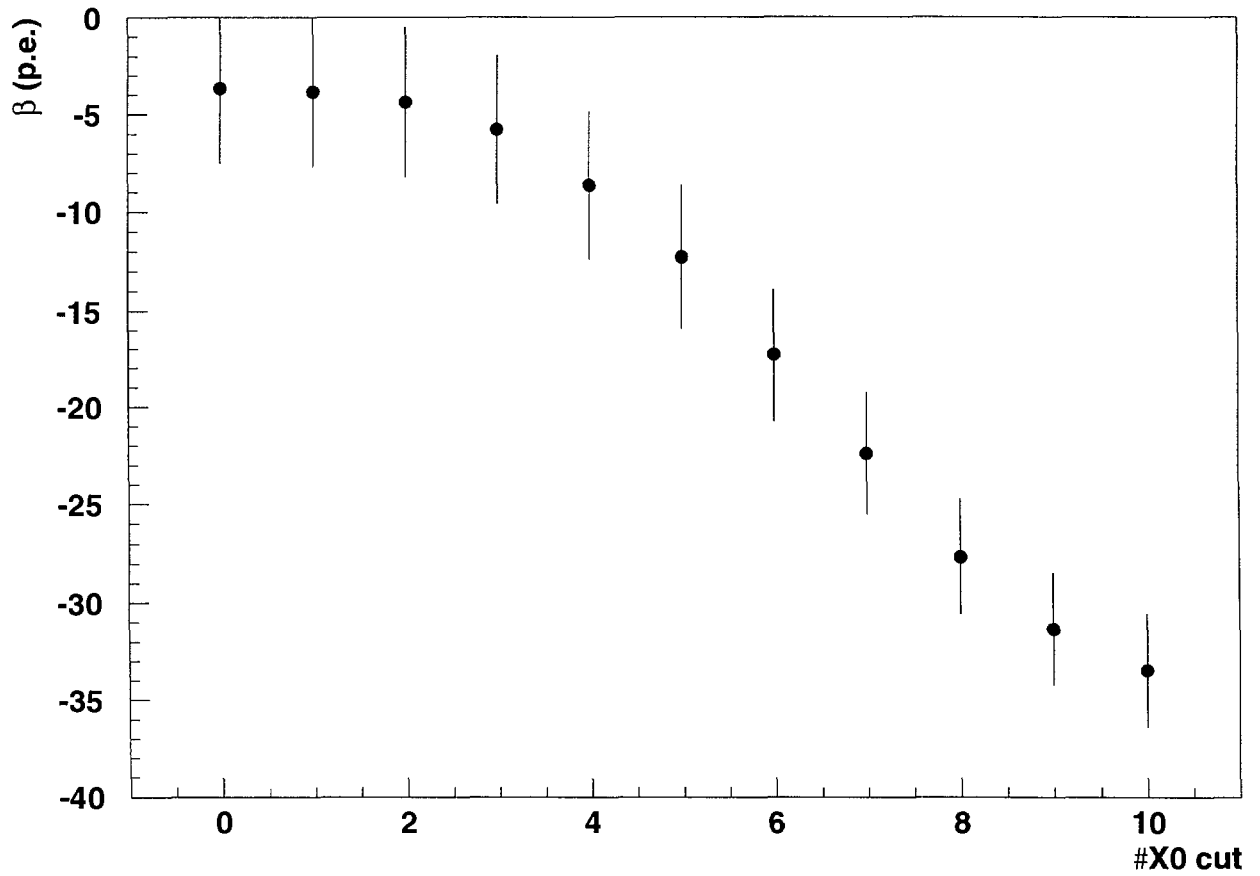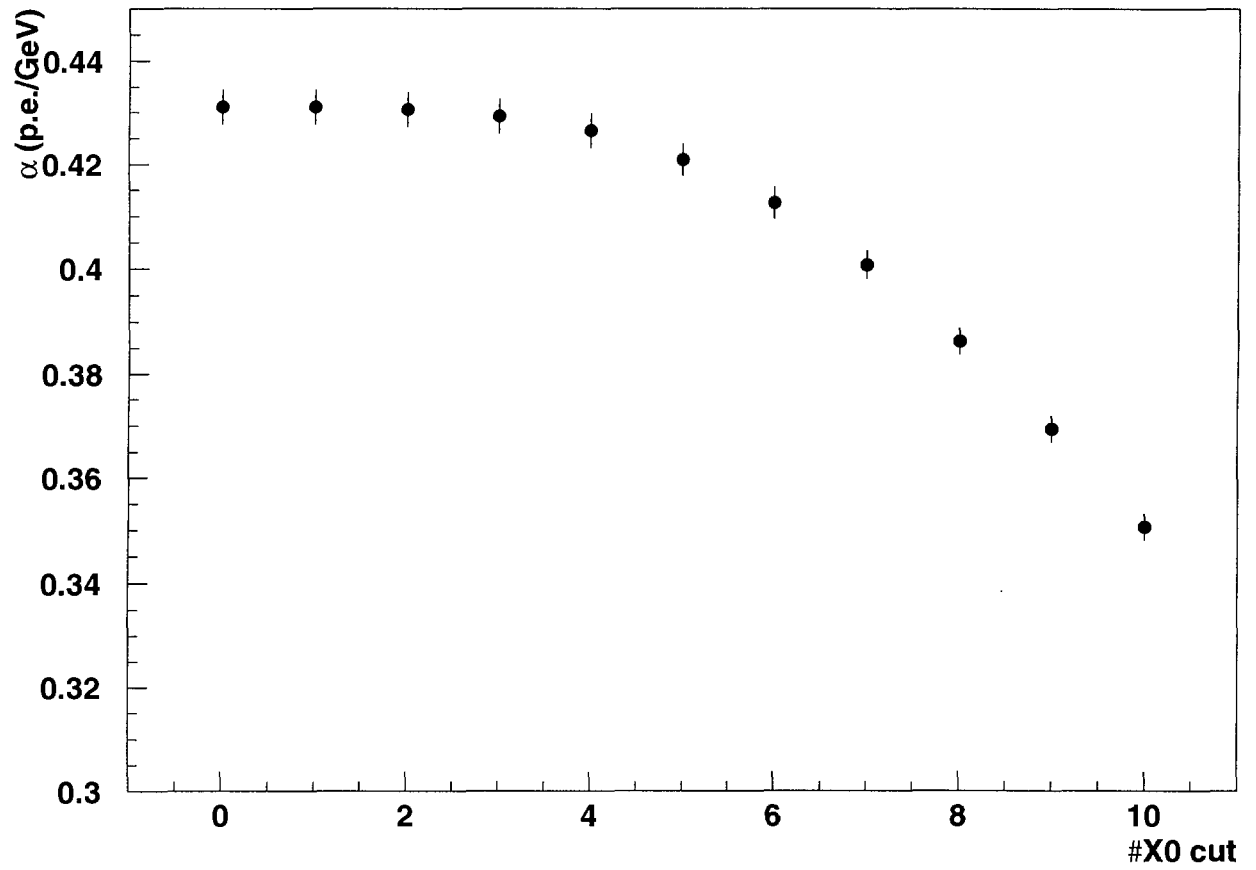
Figure 19

Jet energy reconstruction
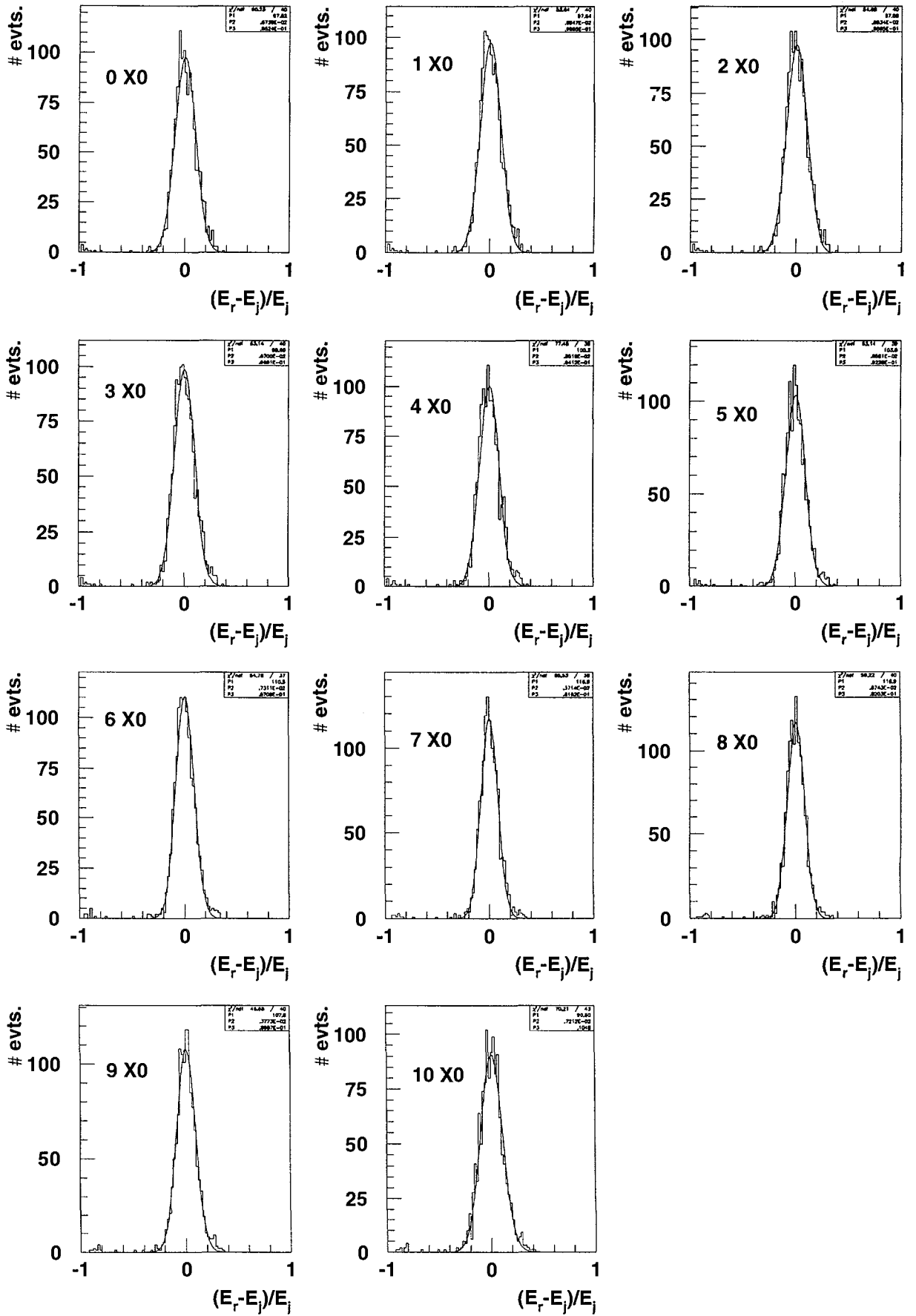
Figure 20

$\langle R \rangle = \langle (E_r - E_j)/E_j \rangle$ vs gamma fraction
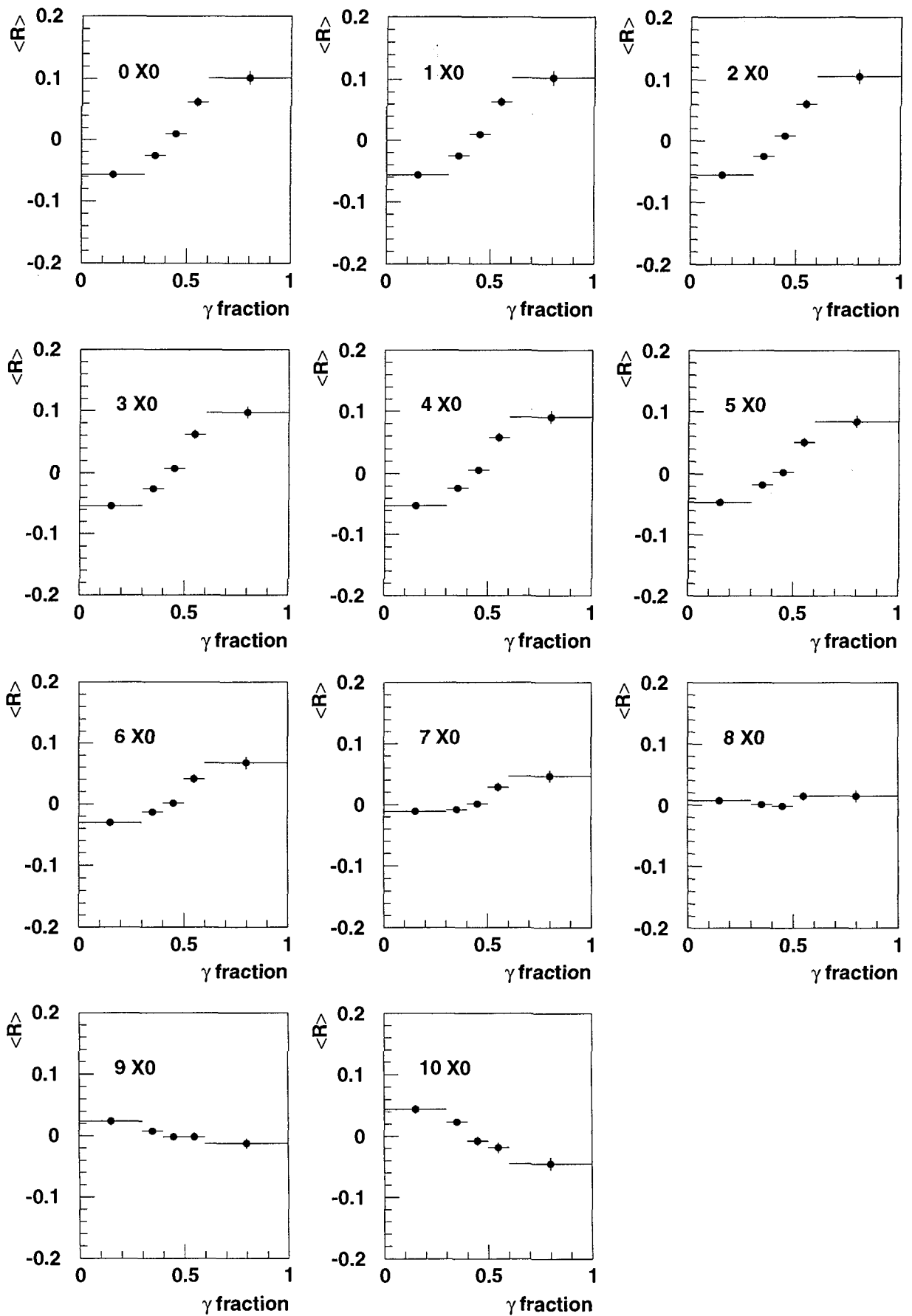
Figure 21

Collected light for jets vs gamma fraction
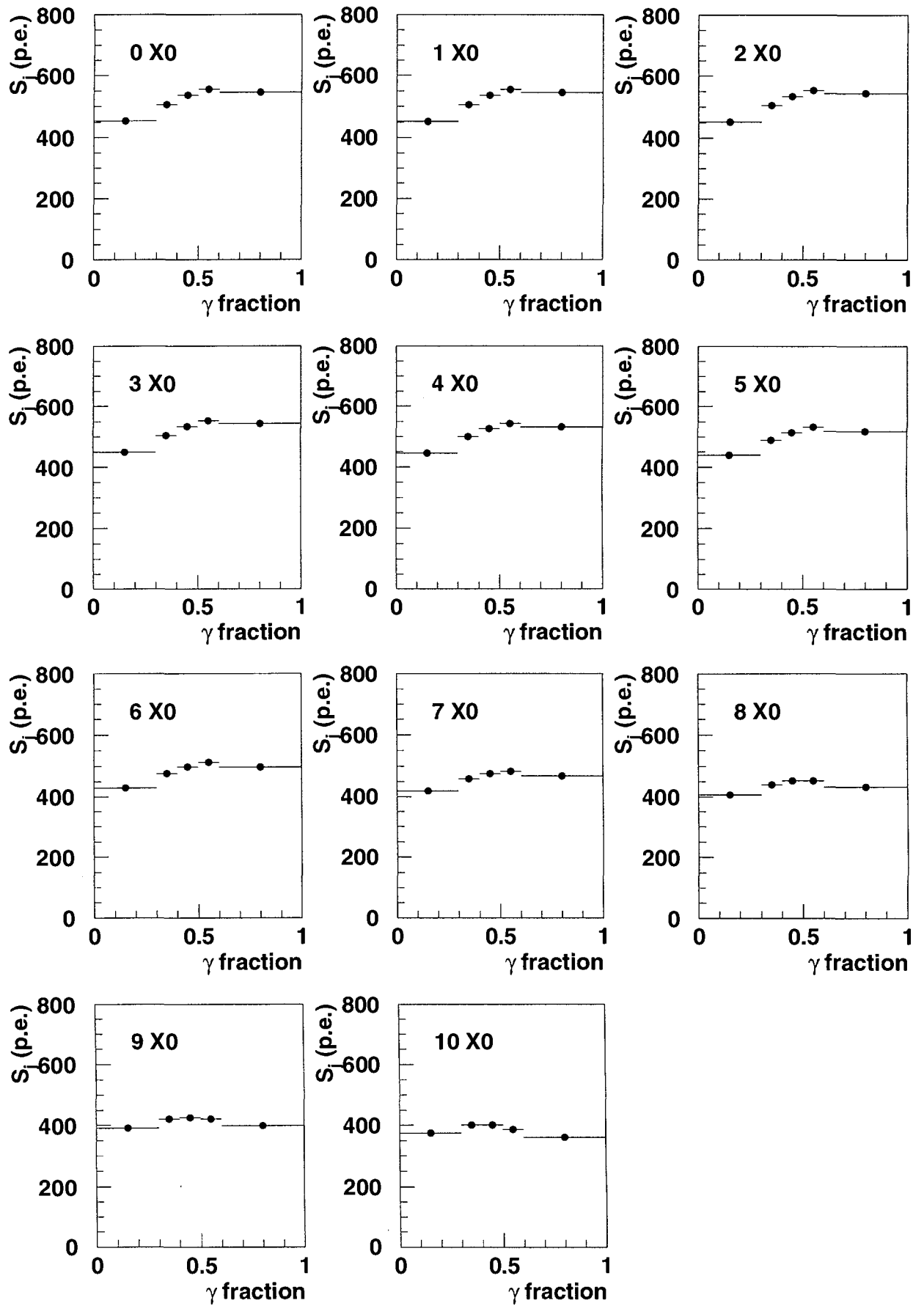
Figure 22

Resolution vs E$_{jet}$
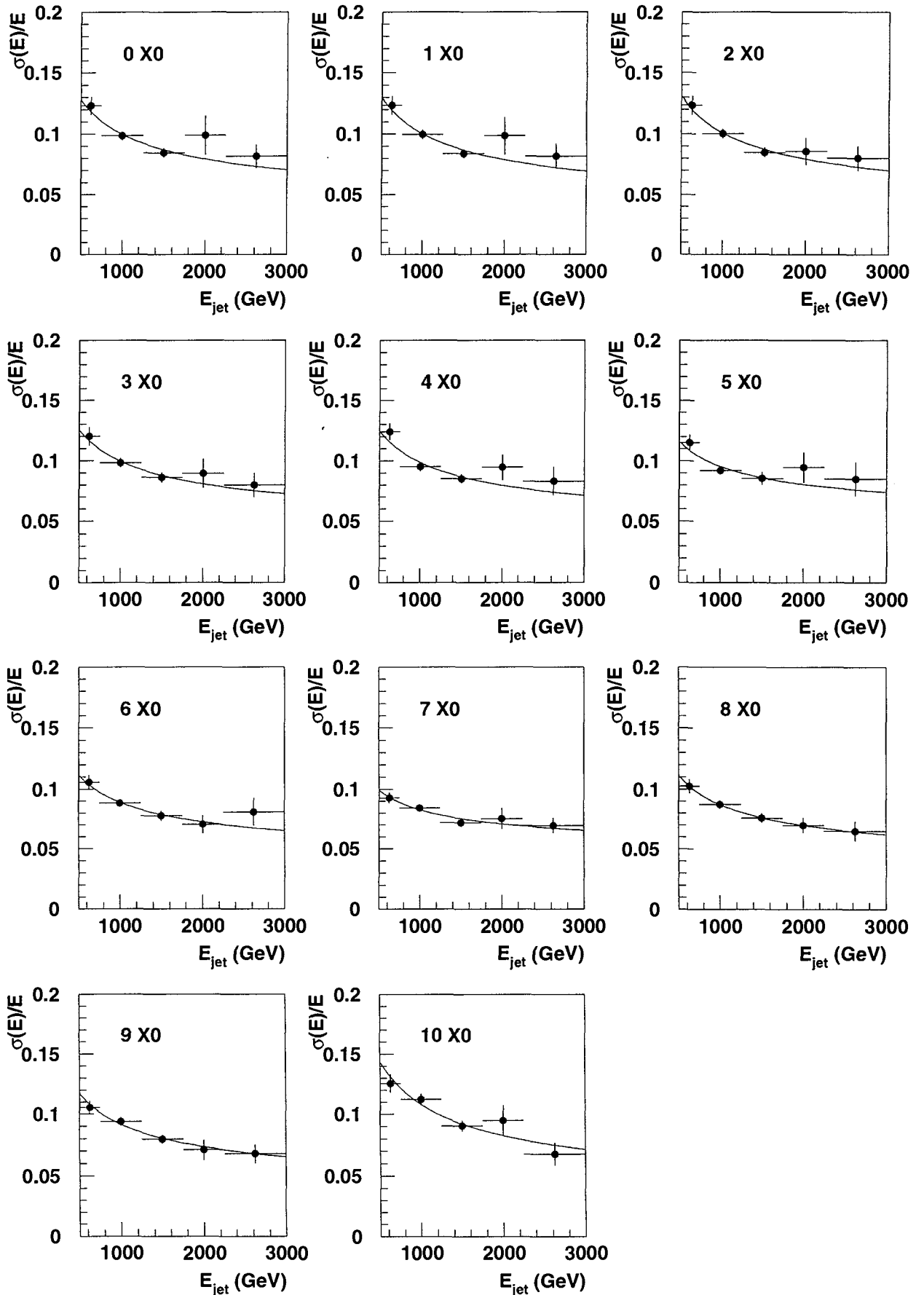
Figure 23
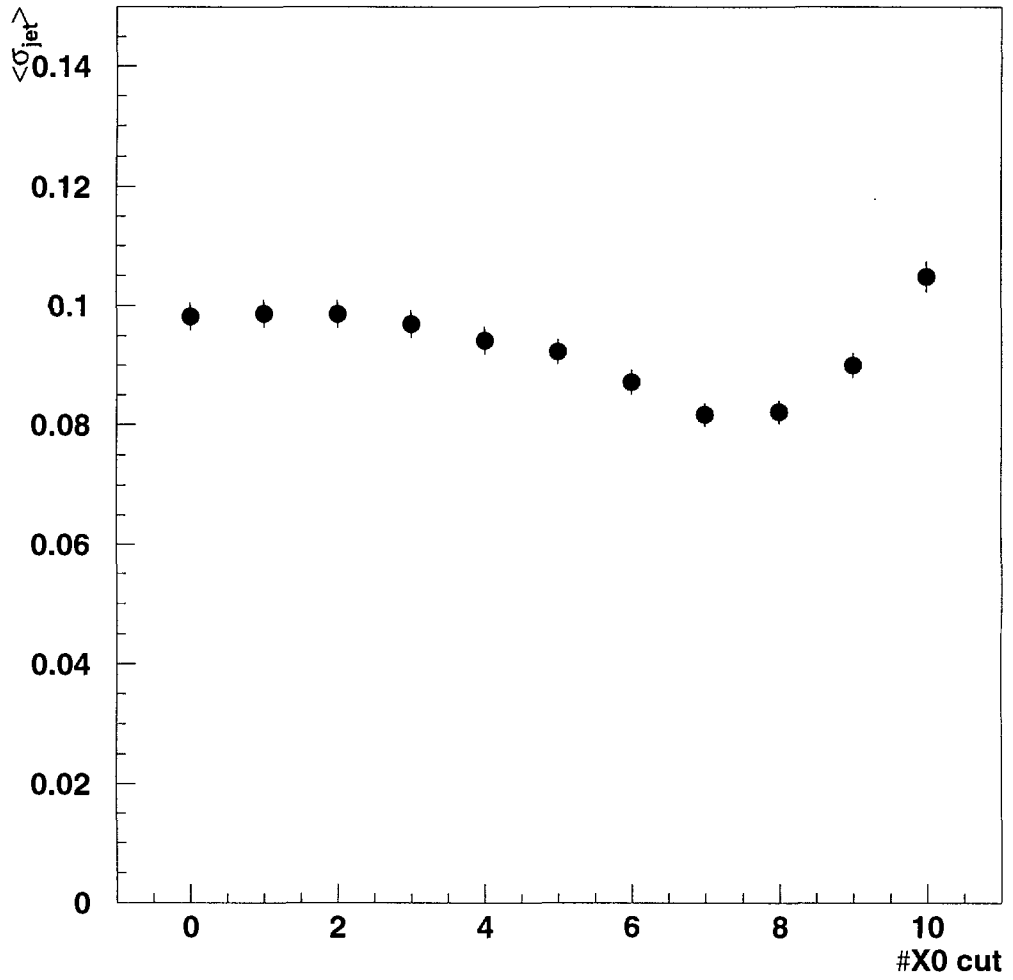
Figure 24

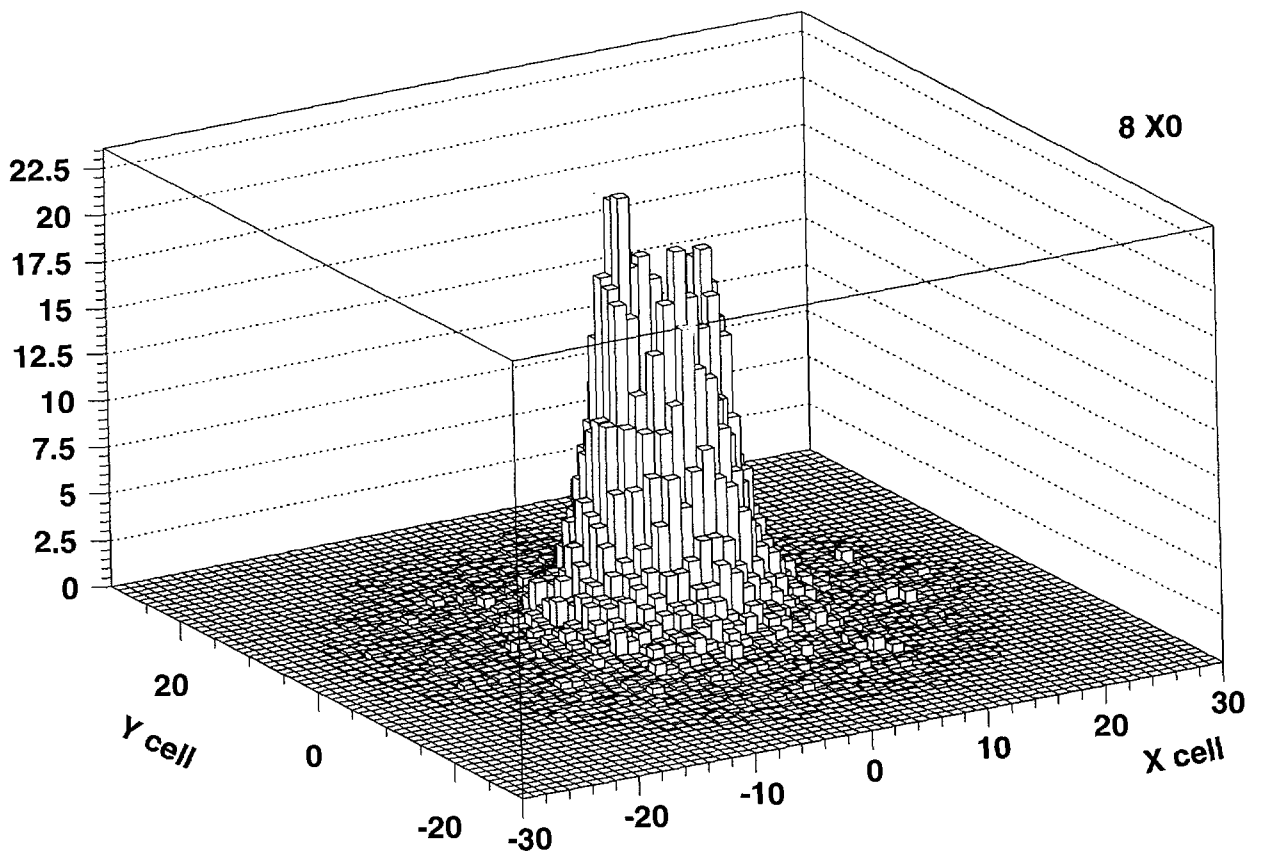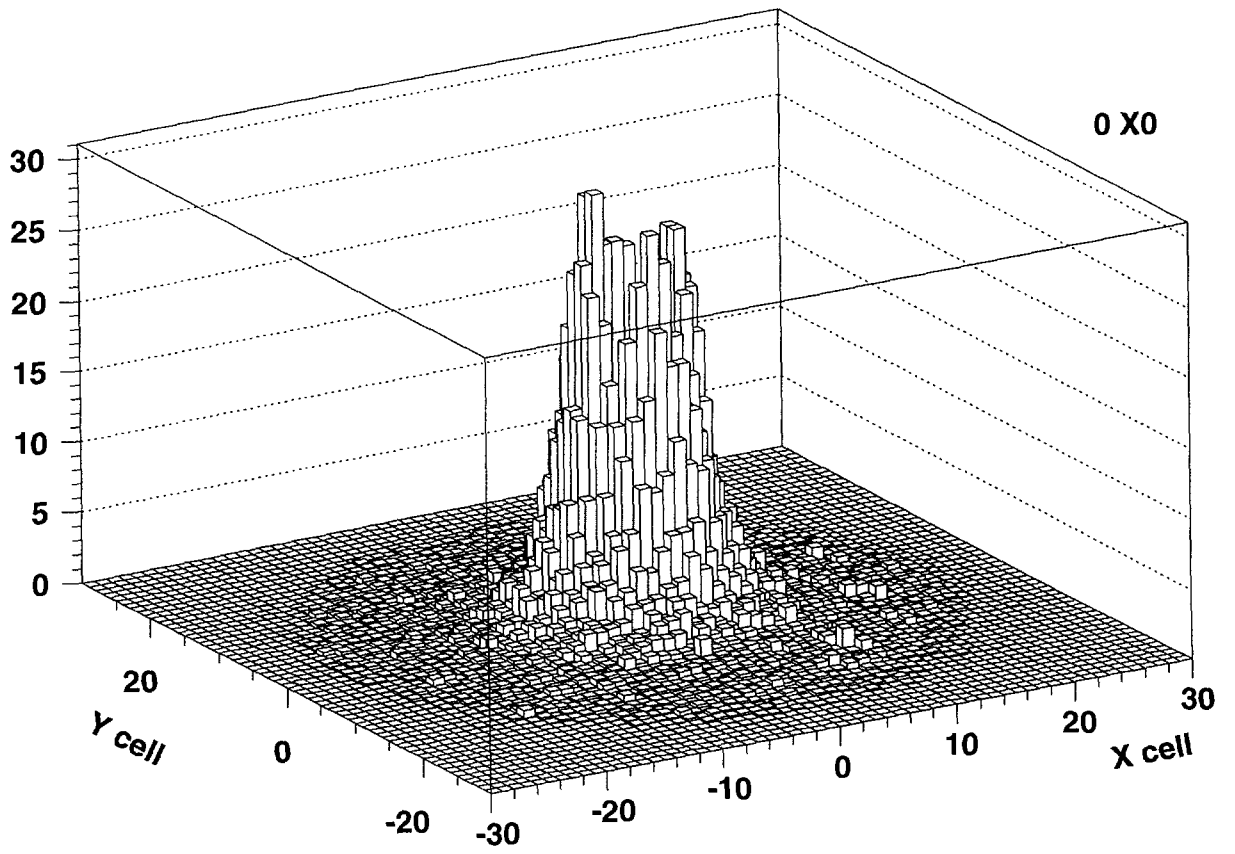# Jet transverse profile
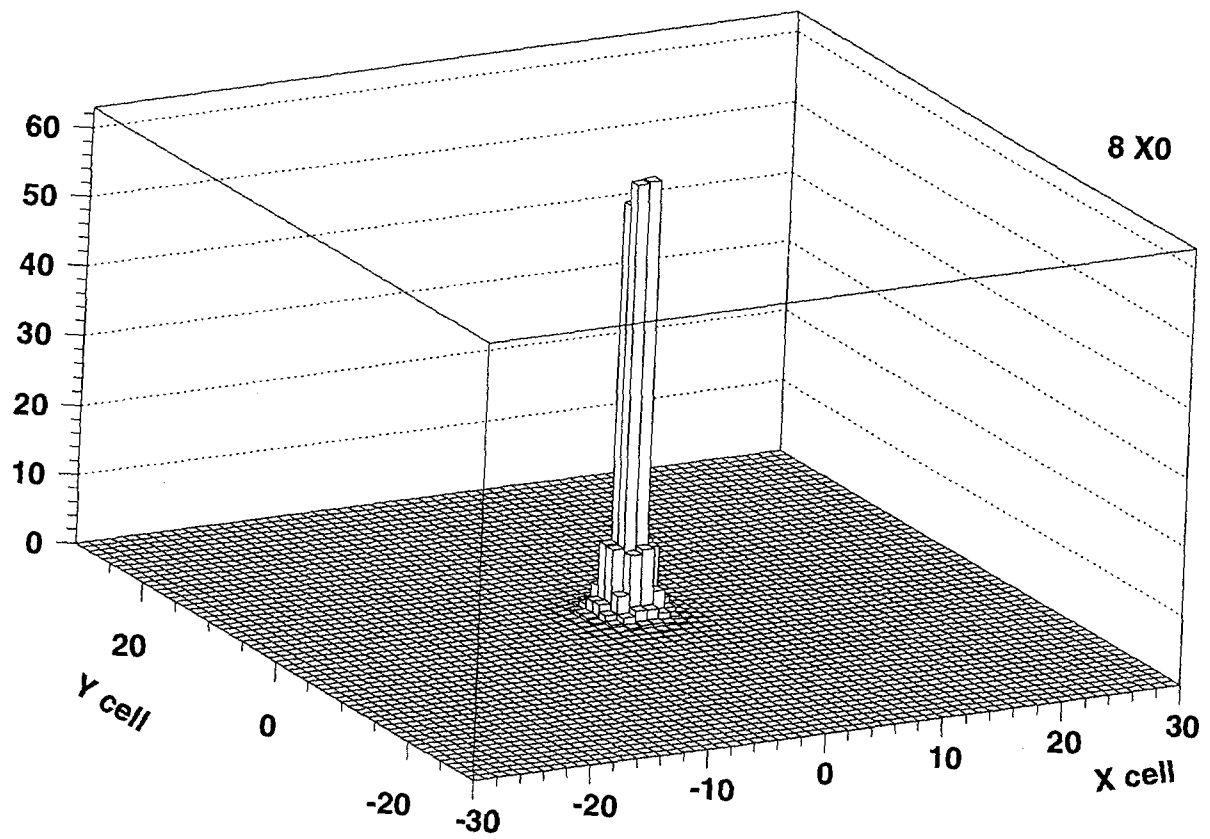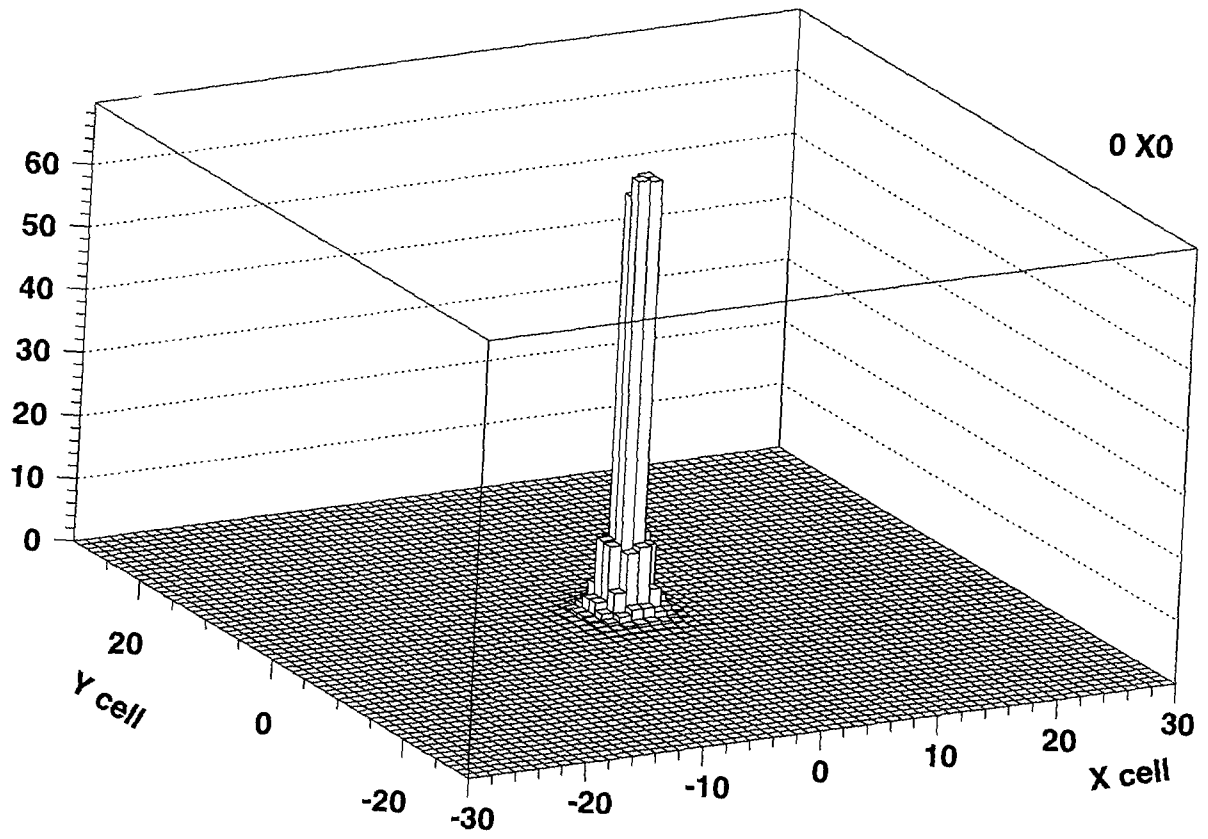
Figure 25

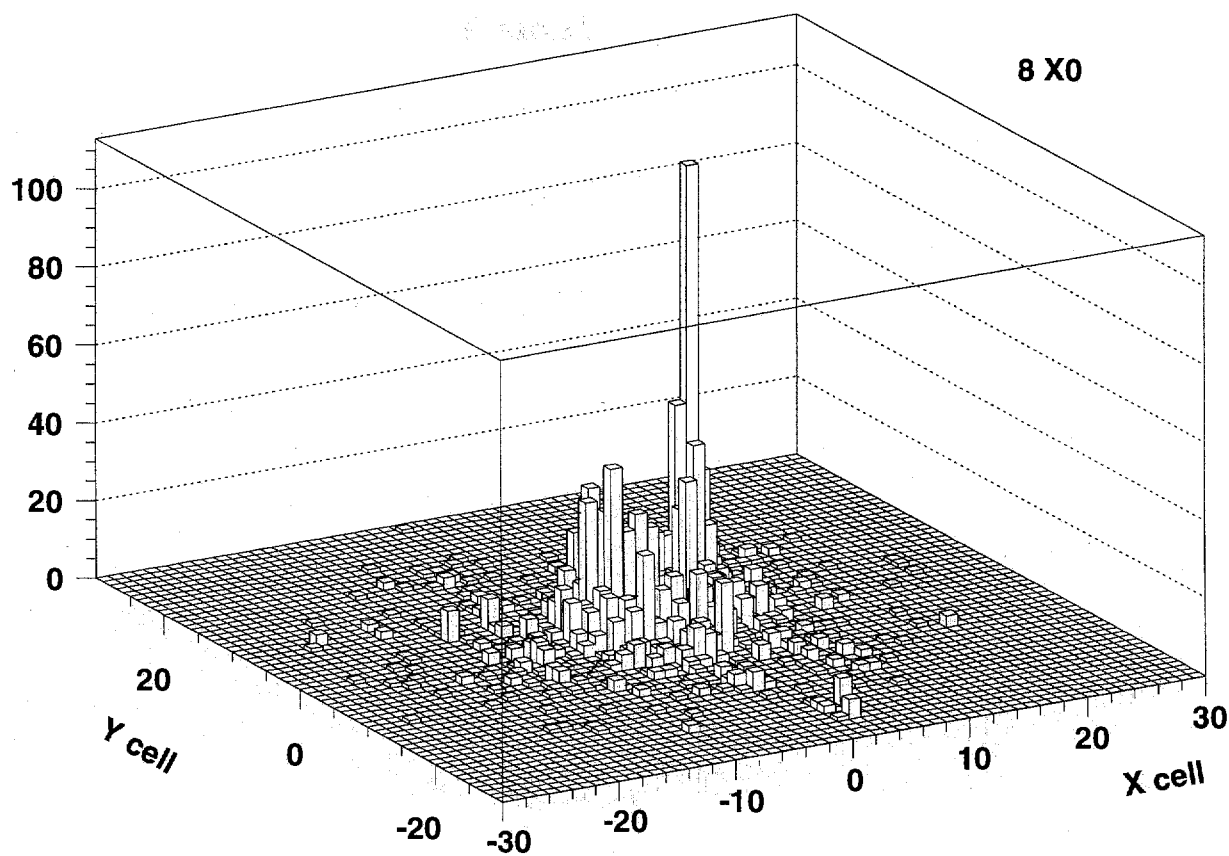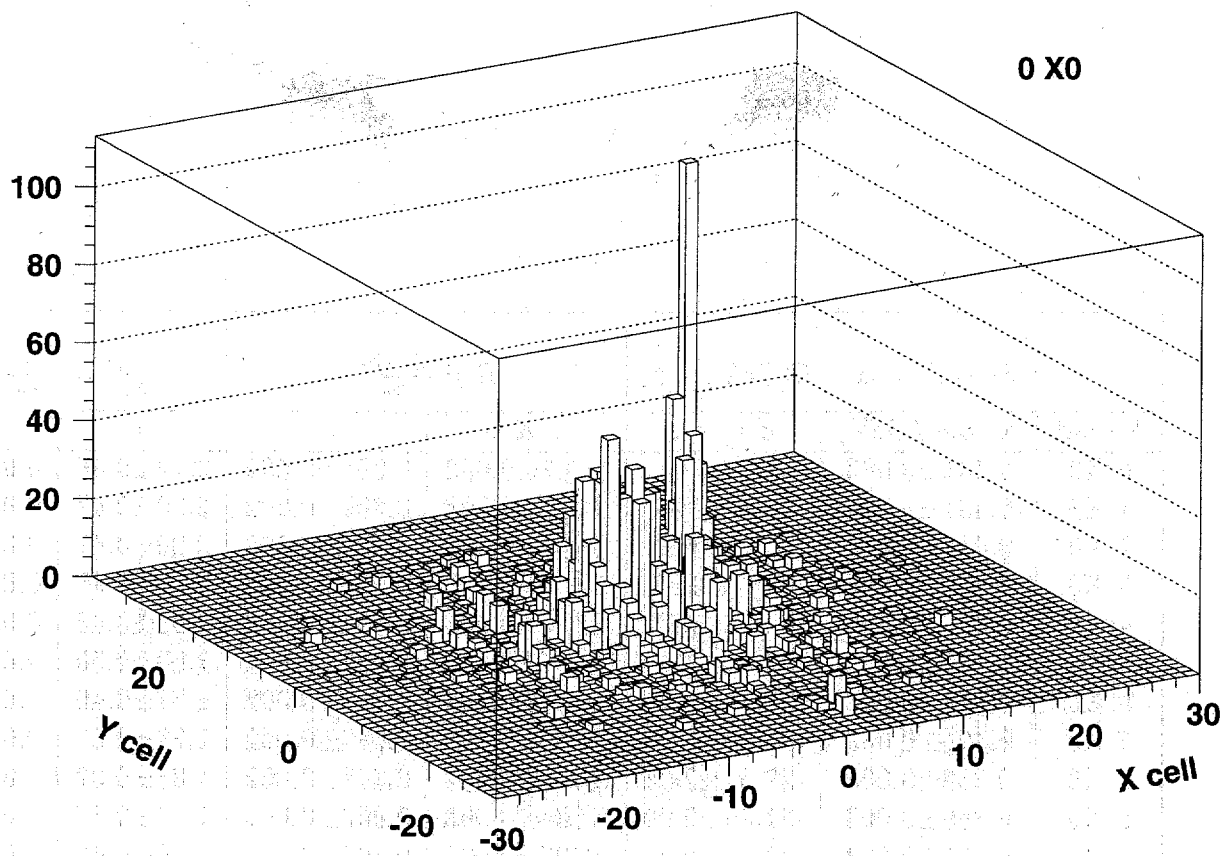## Minimum bias transverse profile

Figure 26

1 TeV jet + MB

0 X0

8 X0

Figure 27